Supporting Information

How well do Conventional Atomistic Simulations predict adsorption binding sites in MOFs compared to Experiment?

Jake Burner[†], Olivier Marchand[†], Sari Warshawsky, Marco Gibaldi, Tom K. Woo[*]

Department of Chemistry and Biomolecular Sciences, University of Ottawa, Ottawa, Ontario K1N 6N5, Canada

[†]These authors contributed equally to this work.

1. Experimental dataset preparation

As a result of an extensive literature search, MOFs which had experimentally resolved binding sites from XRD or neutron diffraction were collected, and isotherms were also collected when available. The dataset was limited to MOFs where the adsorbate atomic positions were fully defined, such that they were available in a crystallographic information file (CIF) format, or similar. Structures where experimental binding sites exhibited a large degree of disorder, or were refined using computational methods (e.g., DFT) were excluded. This decision reflects the fact that DFT results can have systematic biases depending on the choice of functional, basis set, and dispersion corrections that are difficult to deconvolute. Additionally, DFT structures are often obtained from 0 K geometry optimization, which ignores thermal and entropic effects. These calculations are also usually done with at most one adsorbate in the MOF at a time, which neglects effects of guest-guest interactions.

All obtained crystal structures underwent detailed manual inspection and processing to ensure fidelity of the structures to the original reporting publication for GCMC simulations. The processing varied on a case-by-case basis, but included correcting structural disorder, adding missing protons, adjusting incorrect protonation states, etc. As a result of this procedure, roughly fifteen MOFs were excluded since the framework or guest disorder was too severe to be corrected. Various combinations of 27 MOFs with seven different adsorbates (CO_2, C_2H_2, CH_4, NO, Ar, Xe, Kr) across various conditions (temperature,

pressure) were collected for further use in GCMC simulations, given in Table 1 in the main text. The structures were taken either from the CSD or supplementary information provided in the original reporting publications.

2. Computational Details

DFT calculations and GCMC simulations

All MOFs were converted to P1 symmetry and existing guest atoms (from the experimental crystal structure) were removed prior to simulation. All DFT calculations were performed with VASP (version 6.4.2) with the PBE exchange-correlation functional[1] and D3 dispersion corrections[2], and standard VASP pseudopotentials[3] (potpaw.6.4.2), based on the projector augmented wave (PAW) method[4]. For REPEAT[5] calculations and ionic relaxations, k-point sampling was restricted to the gamma point only, an SCF convergence criteria of $1x10^{5}$ eV was used with the VASP default plane-wave cutoff, and a force cutoff of 0.02 eV/Å for ionic relaxations. The positions of the protons were optimized at the DFT level where both the simulation cell and all other atomic positions were fixed. This choice was made since some structures were missing proton positions, so this protocol allowed for structures to be treated more equally. Moreover, proton positions are often poorly resolved due to weak X-ray scattering. For MOF-74(Ni)@NO and CALF-20@H_2O where adsorbates were considered part of the structure (chemisorbed), the adsorbate atom positions were also optimized in addition to all protons. Structures with disorder were fixed using Mercury. For DDEC-6[6] calculations, a plane-wave cutoff energy of 520 eV, and a Γ-centered k-point mesh was used such that the product of the number of k-points and the lattice vector length in each direction was at least 16 Å, as recommended by the manual in the *chargemol* software package.[7] For MOFs with open metal sites, spin-polarized calculations were performed. All GCMC simulations were performed using our in-house code available on GitHub (https://github.com/uowoolab/FastMC-1.4.0). The adsorbates and framework were all treated as rigid, such that only non-bonded interactions were required to be computed. Dispersion/steric interactions were modeled using atom pairwise Lennard-Jones potentials and electrostatic interactions were modelled using fixed atomic partial charges. Lennard-

Jones parameters were obtained from the UFF force field[8], and the resulting binding sites were compared to those obtained from using the DREIDING force field[9] for the framework atoms. The Lennard-Jones parameters and partial atomic charges of the guest molecules used in this work correspond to the following force fields: CO_2[10] C_2H_2[11], H_2O[12], NO[13], CH_4[14], Ar[15], Xe[15], and Kr[15]. Atomic partial charges of framework atoms were fit to the electrostatic potential (ESP) obtained from a single-point DFT calculation using the REPEAT methods, as previously described in the DFT section. For comparison, the resulting binding sites were compared to those obtained when using framework atomic partial charges obtained from MEPO-QEq[16], MEPO-ML[17], and the DDEC[6] methods.

Each GCMC simulation was run until the probability distribution reached a minimum Tanimoto similarity of 0.90, ensuring that adsorption sites were fully sampled. The total number of Monte Carlo steps varied depending on the supercell size and guest-framework interaction strength, ranging approximately from 1.5×10^6 to 4.6×10^8, with a median of about 2.0×10^7 and a mean of roughly 6.6×10^7 steps. The mean value was inflated by a few very long runs; excluding these, the average number of production steps was approximately 2.4×10^7. A cutoff distance of 12.5 Å was applied to all non-bonded interactions. Simulation cells were expanded to fully accommodate this cutoff, and no MOF was simulated using a 1x1x1 unit cell. This ensured that replicate subcells were available for Tanimoto-based convergence analysis. For cases where convergence could not be reached due to local maxima (most notably for the MOF-74 series) parallel simulation were performed. Specifically, 25 independent GCMC simulations of 8.0×10^7 production steps each were executed in parallel, and the resulting probability plots were combined to yield an effective sampling equivalent to approximately 2×10^9 production steps. This procedure reduced wall time to about two days per structure (given the available cores) while maintaining statistical reliability.

Binding site identification

To computationally determine binding sites of MOFs, at each GCMC production step, the 3D atomic coordinates of the adsorbates were stored in a histogram to generate 3D APDs, where regions of high probability correspond to free energy minima. The APDs were stored on a uniform grid of maximum spacing 0.15 Å, and were normalized to unity. The

convergence of the APDs was evaluated by comparing the probability distribution in replicate unit cells within the simulation cell. If the Tanimoto similarity coefficient between replicate unit cells was ≥0.90, the APD was determined to be converged, and the production phase of the simulation was stopped. For most simulations, this required between 10 and 30 million GCMC steps, though certain systems well exceeded 100 million. Once obtained, the APD of the simulation cell was "folded" into a single unit by averaging the APD over all replicate unit cells and renormalized such that the sum of each APD was unity. Binding site positions within the MOF were determined using our in-house GALP method. In this method, a 3D Gaussian filter is applied to each APD to smooth the distributions. Following this, all local maxima are identified and any maxima with a value below 0.05% of the global maximum were discarded. Only the largest maximum within an exclusion radius of 0.40 Å were retained. Next, maxima are vetted according to whether they align with the geometry of the rigid adsorbate molecule used in the GCMC simulation by applying a RMSD-minimizing alignment procedure. This gives the final positions of the binding sites, for which guest-host interaction energies are determined using the respective force fields/charges.

3. Definition of RMSD Metrics

In this work, several RMSD (Root Mean Square Deviation) metrics are reported to quantify differences between binding site configurations. The atom-centred RMSD, reported in Table 1, is computed from the displacements of all guest atoms across the ensemble of binding sites, excluding the MOF framework, and reflects the overall atomic-level mismatch between two configurations. A guest-centred mean RMSD is also reported in the RMSD files provided with the Zenodo dataset. This quantity corresponds to the average of the RMSDs computed independently for each binding-site pair, such that each binding site contributes equally. In addition, a center-of-mass (COM) RMS Euclidean displacement is included to capture purely translational differences between binding sites, independent of internal molecular distortions or rotations, and is also reported in Table 1. Since all comparisons involve the same guest molecule and the same number of binding sites, the guest-centred RMSD (RMS) is identical to the atom-centred RMSD and is therefore not reported separately.

4. Binding Energy Cross-Comparison Between Force Fields and Charge Methods

The pairwise RMSE matrix (Figure S4) compares the binding energies predicted for each mapped binding site across 34 MOF-guest systems, excluding MOF-74(Zn) and MOF-74(Fe) as described in the main text. Within each forcefield, the three charge methods yield closely aligned energies, with UFF showing intra-set RMSEs of 0.33-0.50 kcal mol^{-1} and DREIDING showing 0.33-0.54 kcal mol^{-1}. In contrast, the deviations between UFF and DREIDING are considerably larger, typically 0.78-0.97 kcal mol^{-1}. This clustering by force field indicates that differences in the Lennard-Jones parameters, rather than the charge model, dominate variation in the computed binding energies.

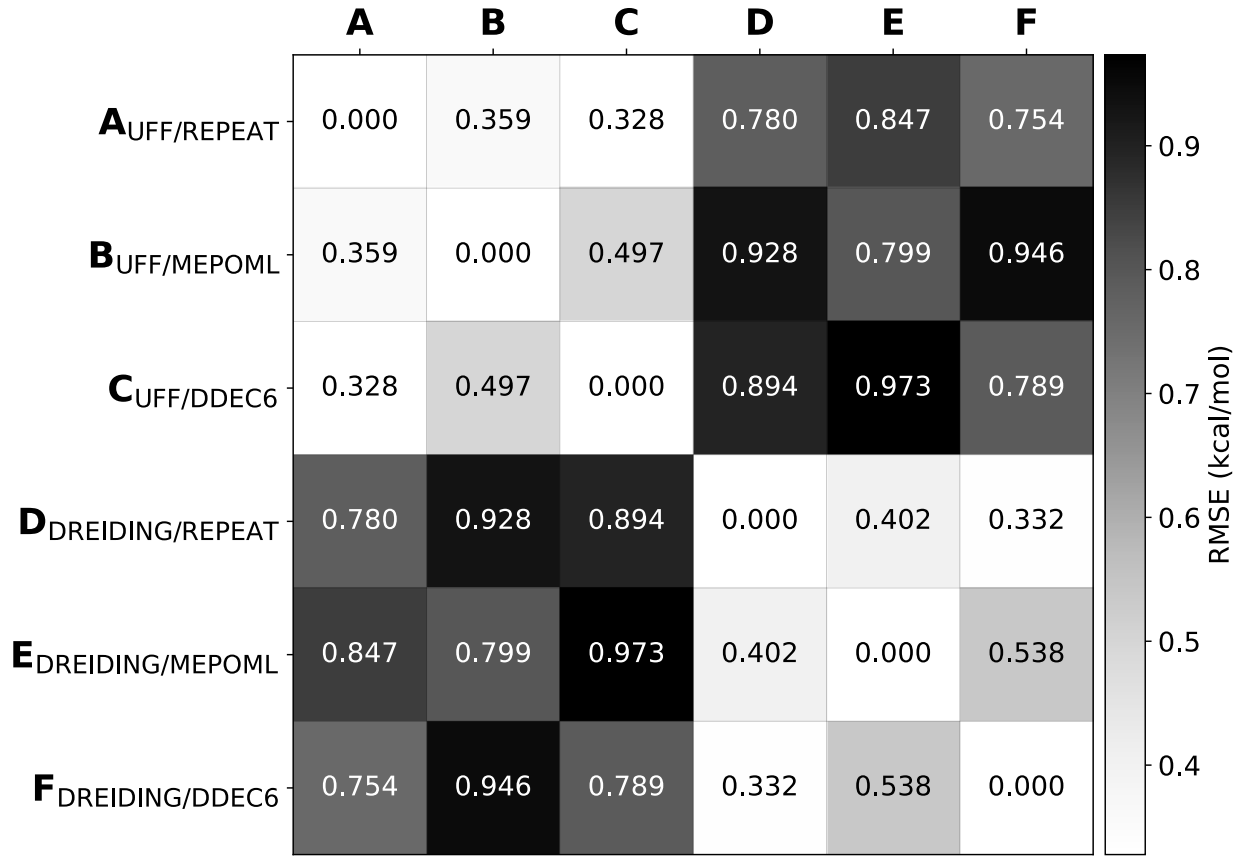

Figure S1. Pairwise RMSE (kcal mol^{-1}) of binding energies across different force fields (UFF, DREIDING) and charge methods (REPEAT, MEPO-ML, DDEC6). Lower values along the diagonal blocks indicate consistency with each force field, while higher cross0field values reflect differences in the Lennard-Jones parameters.

5. Dataset Availability

The CIF files for each MOF in the dataset, along with their corresponding atomic charges, are available on Zenodo at https://zenodo.org/records/17994717. The binding site outputs generated using our in-house GALP (https://github.com/uowoolab/GALP) code, together with the folded adsorption density profiles, are also provided for each MOF and for each force field/charge combination: UFF/REPEAT, UFF/DDEC6, UFF/MEPO-ML, DREIDING/REPEAT, DREIDING/DDEC6, and DREIDING/MEPO-ML. These datasets can be accessed on Zenodo at https://zenodo.org/records/17994722.

6. Supporting Tables and Figures

Table S1. Comparison of isosteric heats of adsorption (Q_{st}) of MOF-74 obtained from simulation and experiment at a coverage of ~0.1 CO_2 per M^{2+}.

MOF	Simulated heat of adsorption (kJ/mol)	Experimental heat of adsorption (kJ/mol)
MOF-74(Zn)	24.1	26.8
MOF-74(Fe)	25.6	33.2
MOF-74(Co)	24.1	33.6
MOF-74(Mg)	30.1	43.5

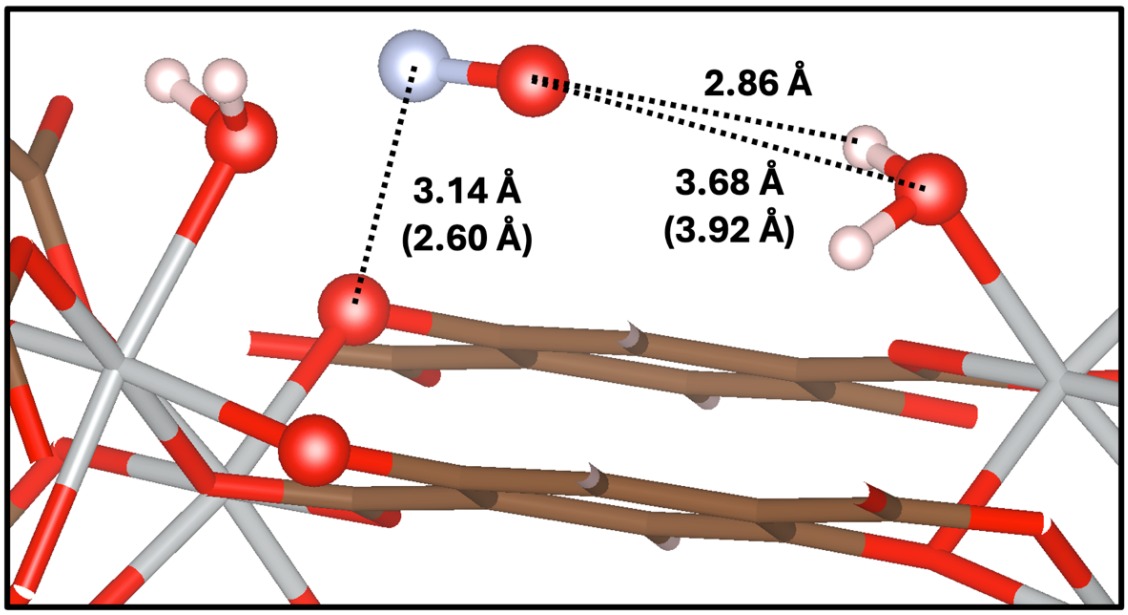

Figure S2. Physisorptive NO binding site in MOF-74(Ni) determined by GCMC, where 100% of OMSs are capped by water. Values in parentheses are distances obtained from one of the experimental crystal structures reported in the publication (CCDC refcode UJOCEF).[18] The simulation conditions were 196 K, 0.40 bar NO. Atomic positions of capping sites and protons were optimized at the PBE level prior to simulation.

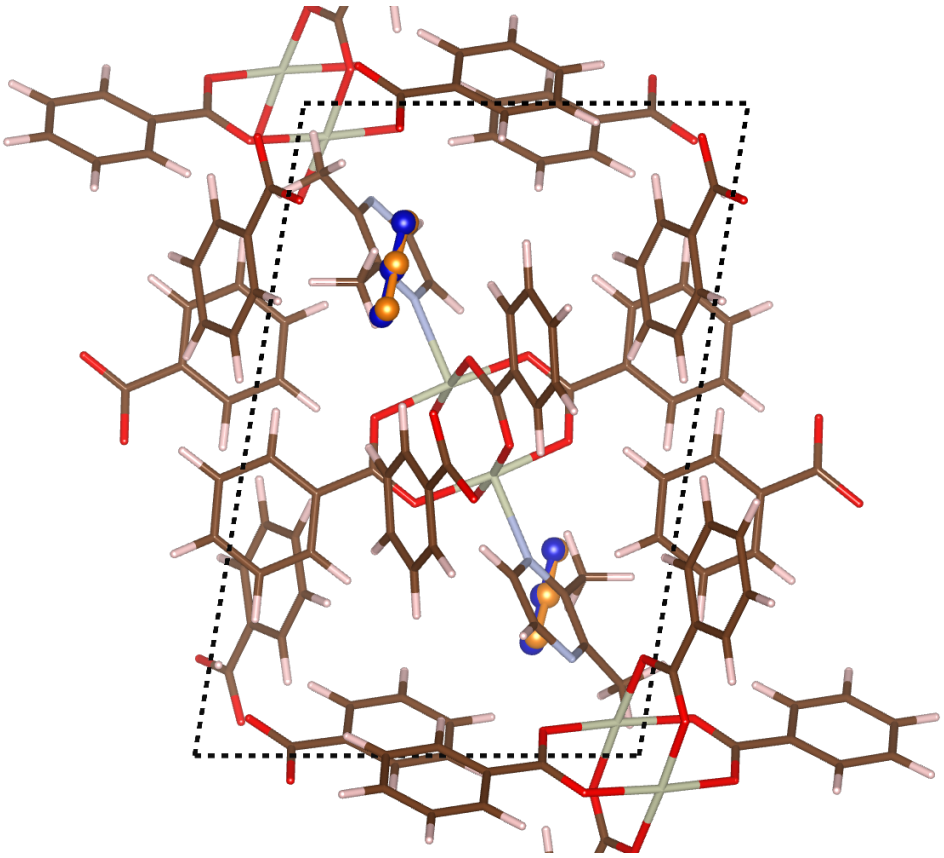

Figure S3. Comparison of binding site positions (experimental and simulated at 90 K, 1 bar) of CO_2 in $[Rh_2(bza)_4(dimethyl\text{-}pyz)]_n$. Experimental binding sites are shown as orange spheres, and simulated binding sites are shown as blue spheres.

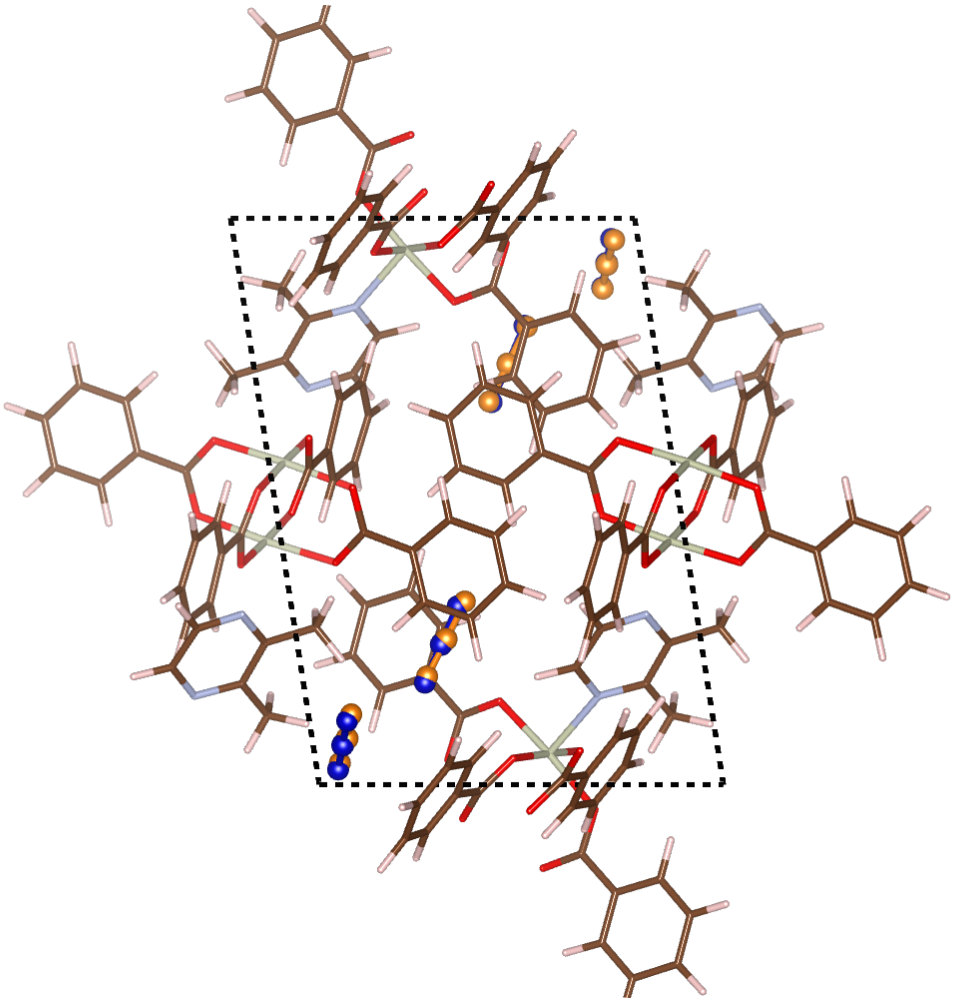

Figure S4. Comparison of binding site positions (experimental and simulated at 90 K, 17 bar) of CO_2 in $[Rh_2(bza)_4(dimethyl\text{-}pyz)]_n$. Experimental binding sites are shown as orange spheres, and simulated binding sites are shown as blue spheres.

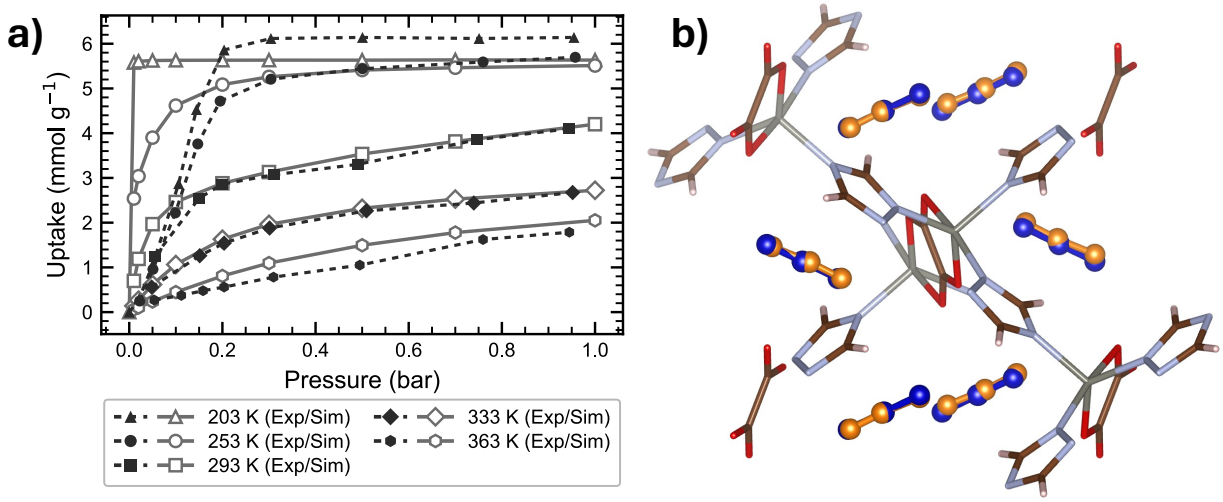

Figure S5. Comparison of binding site positions (experimental and simulated at 298 K, 10 bar) with CO_2 adsorption isotherms measured at 203 K, 253 K, 293 K, 333 K and 363 K for CALF-20. Experimental binding sites are shown as orange spheres, and simulated binding sites are shown as blue spheres.

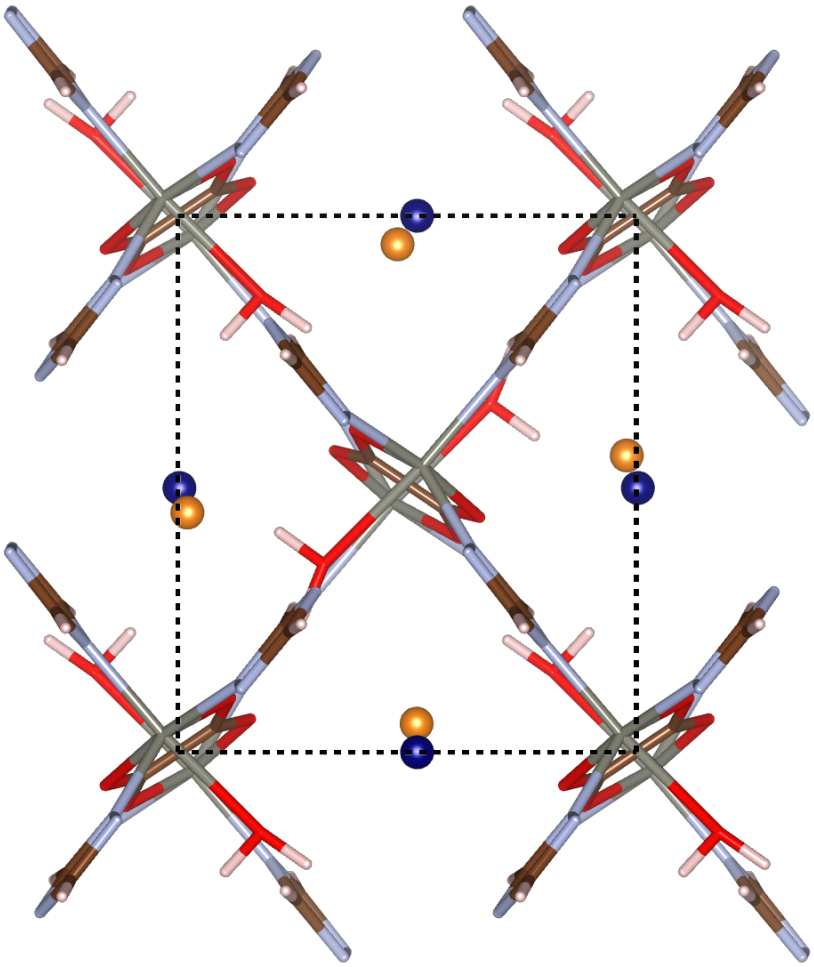

Figure S6. Comparison of binding site positions (experimental and simulated at 296 K, 100% relative humidity) of H_2O in calf-20. Experimental binding sites are shown as orange spheres, and simulated binding sites are shown as blue spheres. *Hydrogens are excluded from the comparison since experimental data did not report orientation*.

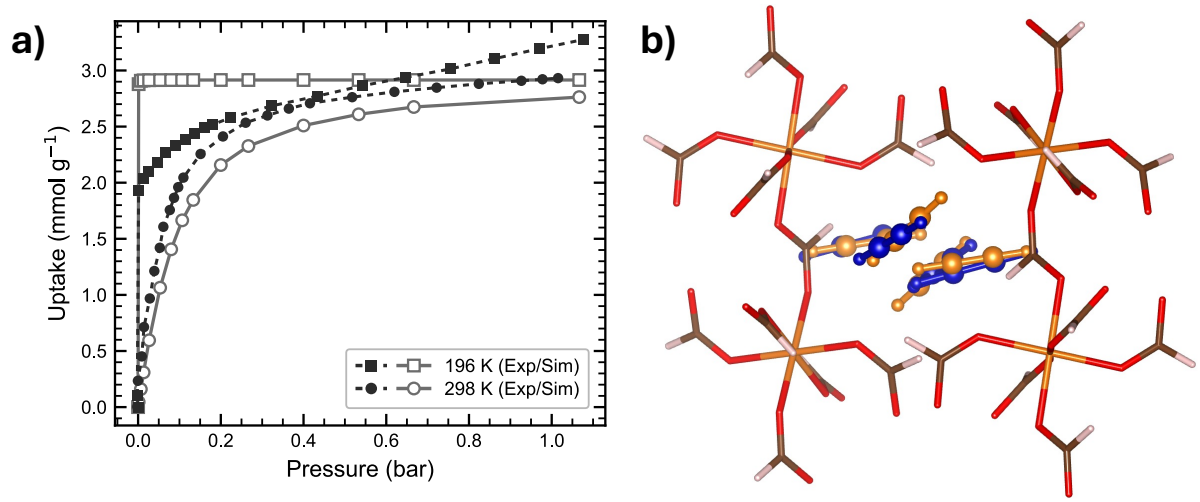

Figure S7. Comparison of binding site positions (experimental and simulated at 90 K, 1.01 bar) with C_2H_2 adsorption isotherms measured at 196 K and 298 K for $Mg(HCOO)_2$. Experimental binding sites are shown as orange spheres, and simulated binding sites are shown as blue spheres.

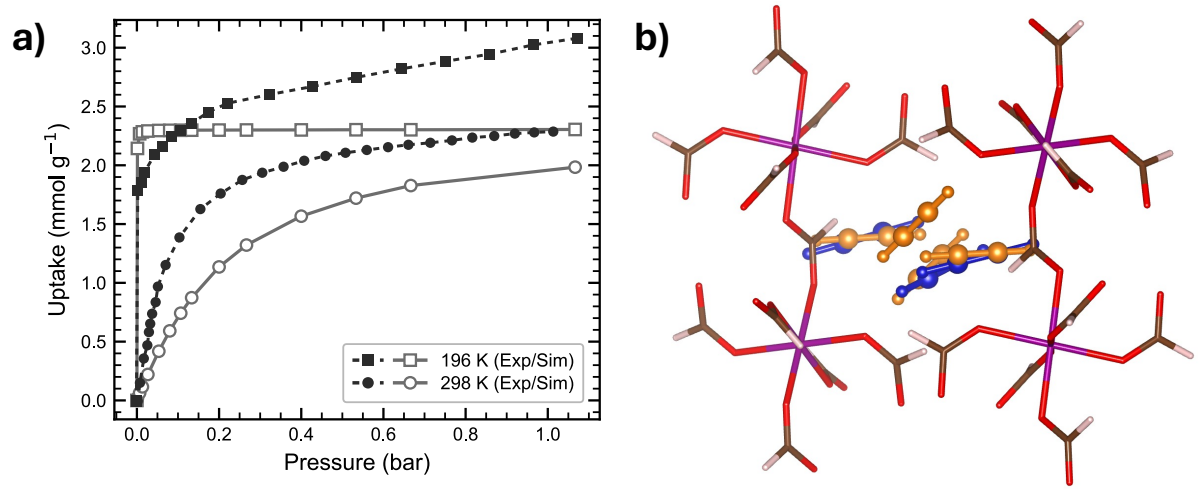

Figure S8. Comparison of binding site positions (experimental and simulated at 90 K, 1.01 bar) with C_2H_2 adsorption isotherms measured at 196 K and 298 K for $Mn(HCOO)_2$. Experimental binding sites are shown as orange spheres, and simulated binding sites are shown as blue spheres.

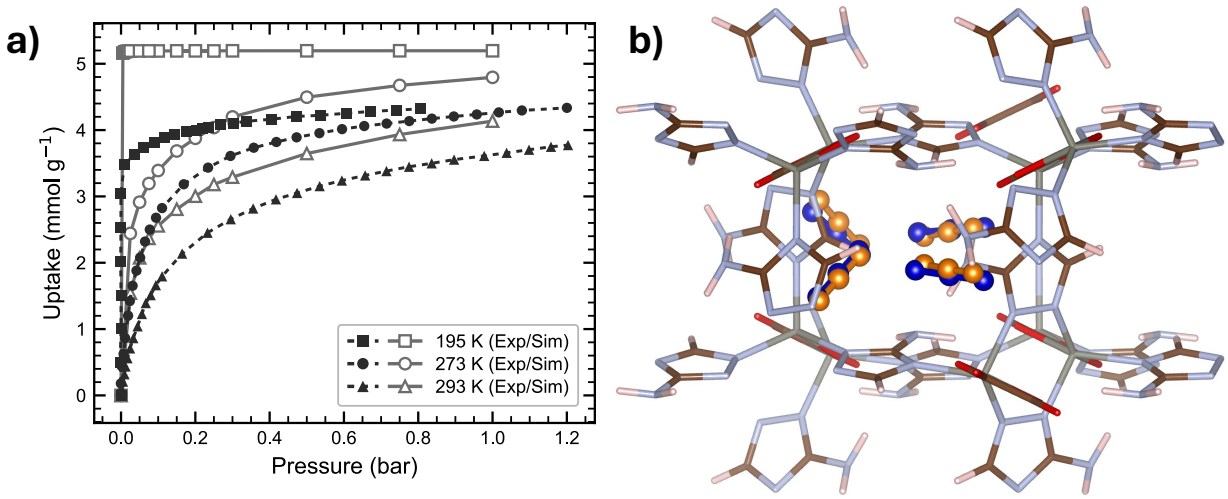

Figure S9. Comparison of binding site positions (experimental and simulated at 173 K, 0.85 bar) with CO_2 adsorption isotherms measured at 195 K, 273 K and 293 K for CALF-15. Experimental binding sites are shown as orange spheres, and simulated binding sites are shown as blue spheres.

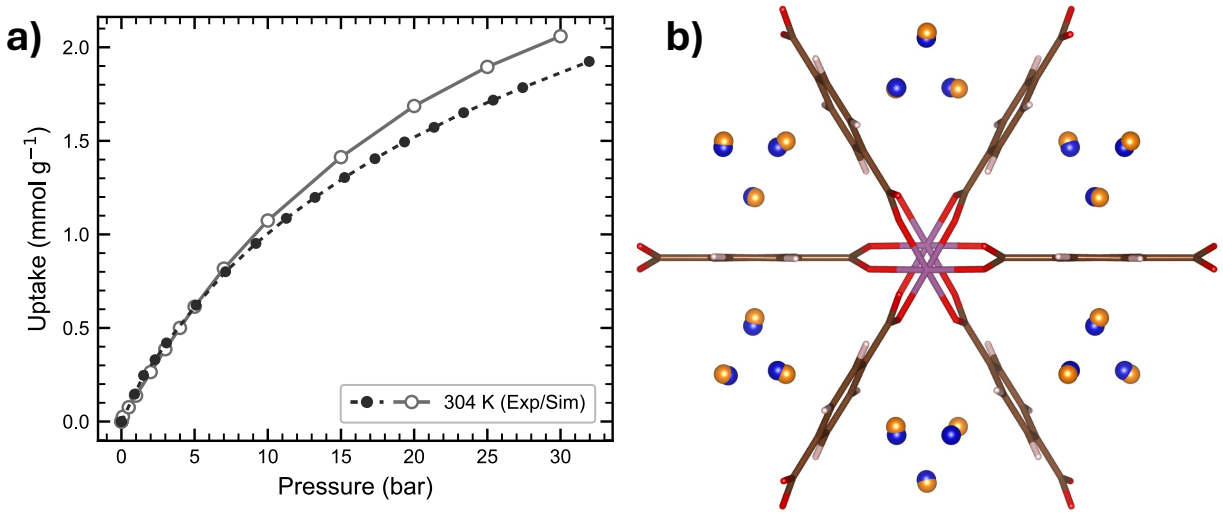

Figure S10. Comparison of binding site positions (experimental and simulated at 230 K, 9 bar) with CH_4 adsorption isotherms measured at 304 K for $Sc_2(BDC)_3$. Experimental binding sites are shown as orange spheres, and simulated binding sites are shown as blue spheres.

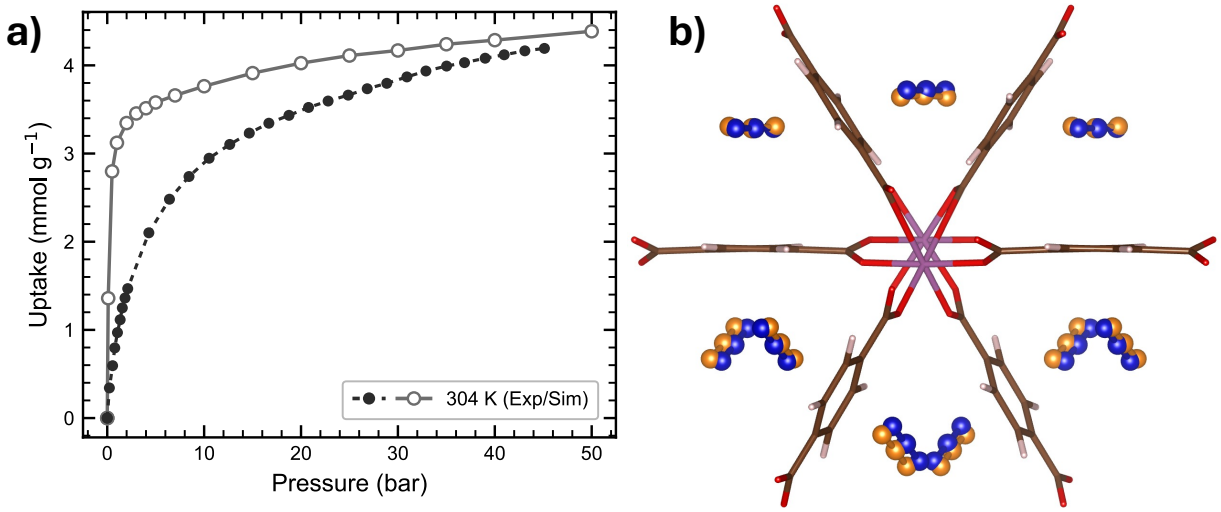

Figure S11. Comparison of binding site positions (experimental and simulated at 235 K, 1 bar) with CO_2 adsorption isotherms measured at 304 K for $Sc_2(BDC)_3$. Experimental binding sites are shown as orange spheres, and simulated binding sites are shown as blue spheres.

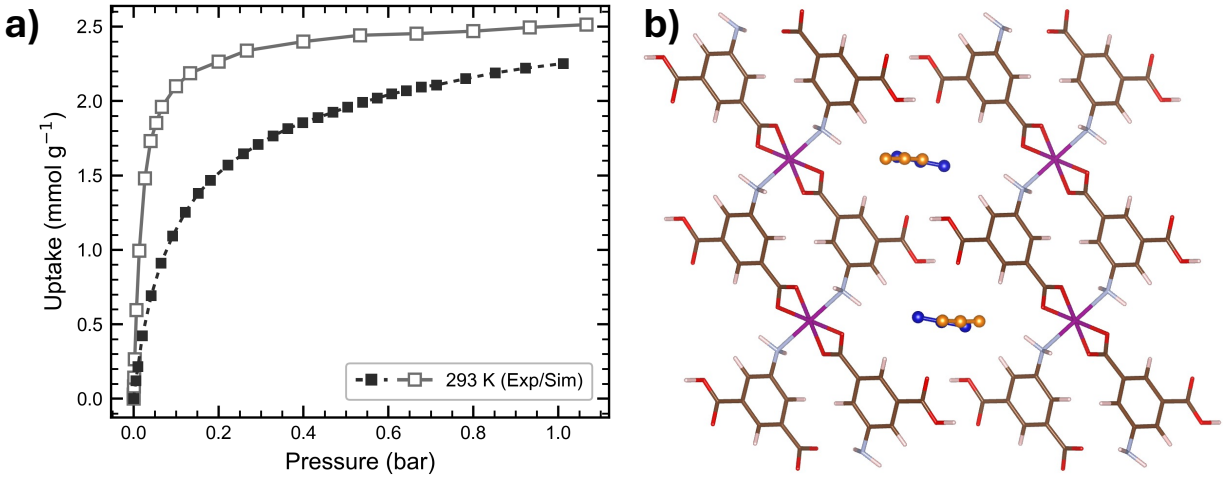

Figure S12. Comparison of binding site positions (experimental and simulated at 293 K, 1.1 bar) with CO_2 adsorption isotherms measured at 293 K for MUF-16(Mn). Experimental binding sites are shown as orange spheres, and simulated binding sites are shown as blue spheres.

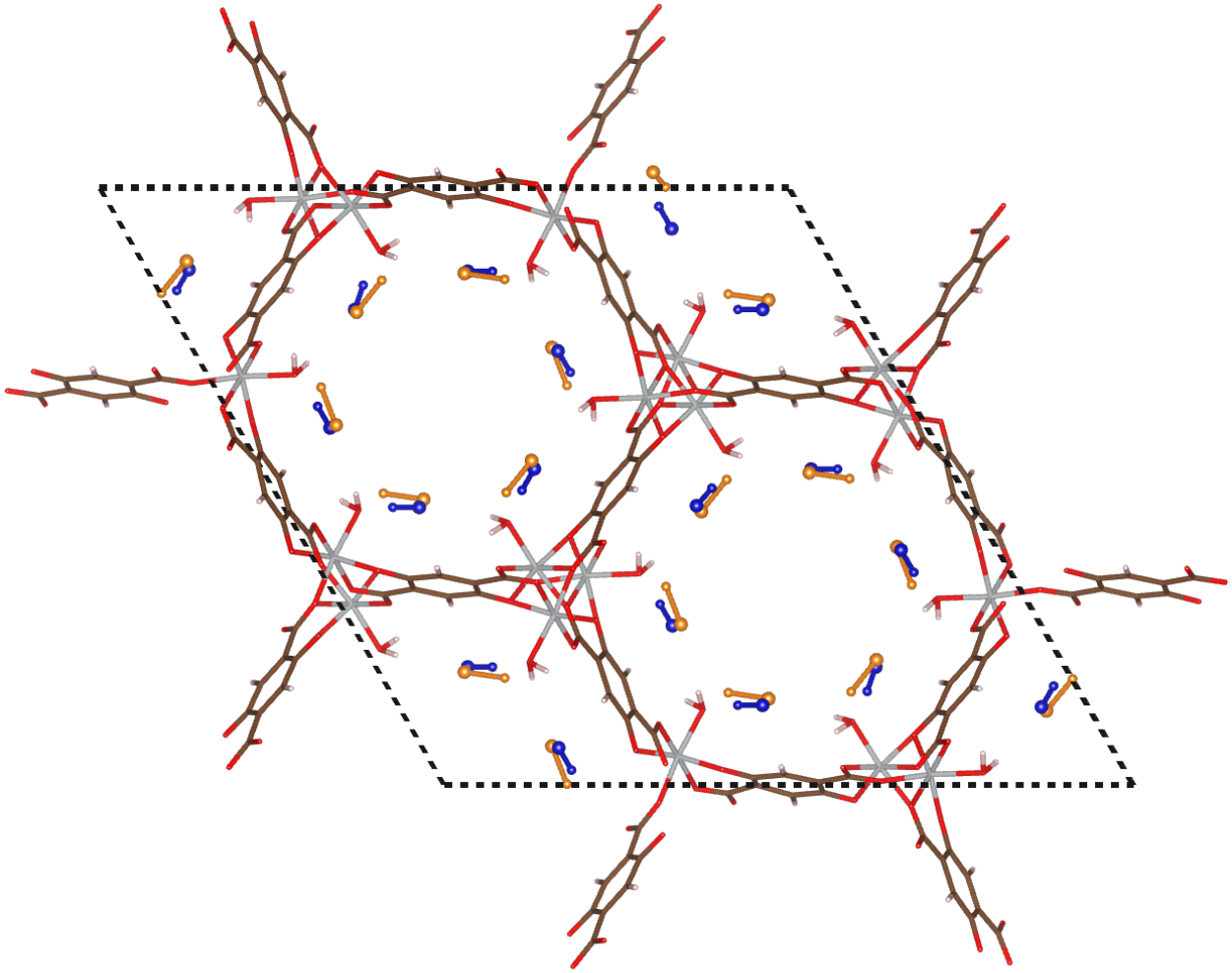

Figure S13. Comparison of binding site positions (experimental and simulated at 196 K, 0.4 bar) of NO in MOF-74(Ni) (H_2O capped). Experimental binding sites are shown as orange spheres, and simulated binding sites are shown as blue spheres. The nitrogen atoms are represented as smaller spheres to distinguish orientation.

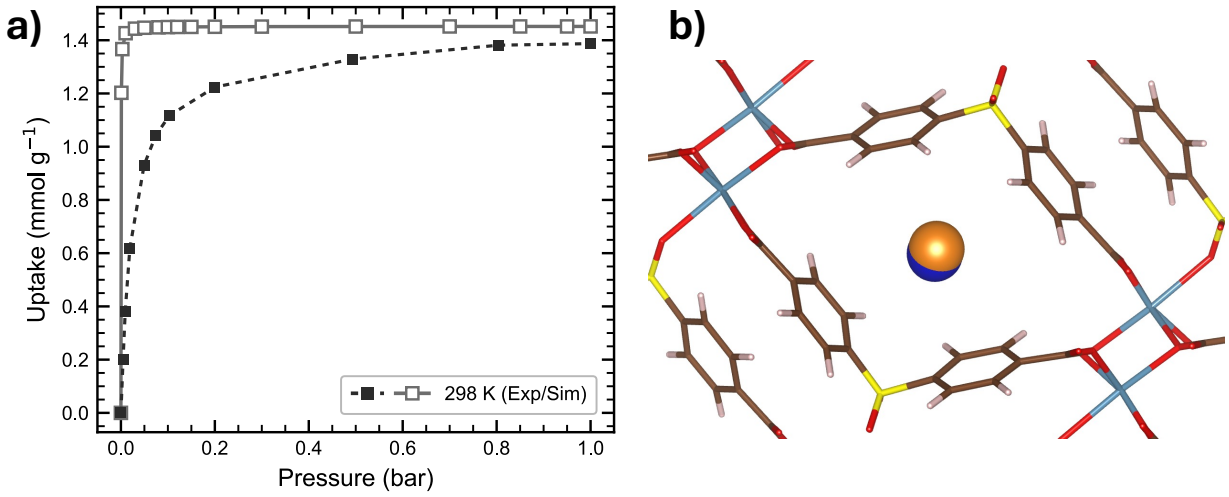

Figure S14. Comparison of binding site positions (experimental and simulated at 298 K, 1 bar) with Xe adsorption isotherms measured at 298 K for SBMOF-1. Experimental binding sites are shown as orange spheres, and simulated binding sites are shown as blue spheres.

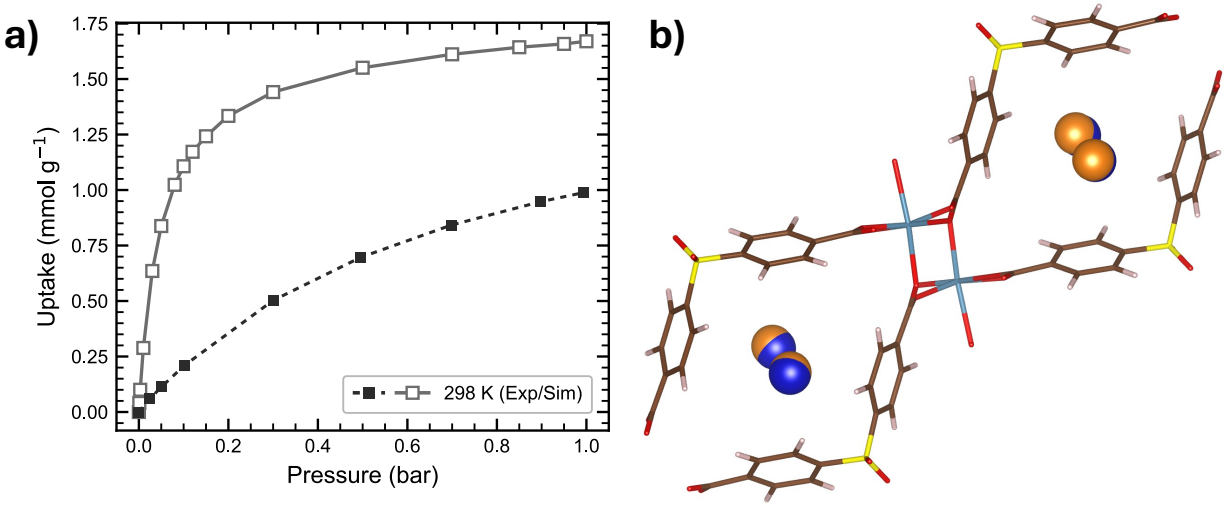

Figure S15. Comparison of binding site positions (experimental and simulated at 298 K, 1 bar) with Kr adsorption isotherms measured at 298 K for SBMOF-1. Experimental binding sites are shown as orange spheres, and simulated binding sites are shown as blue spheres.

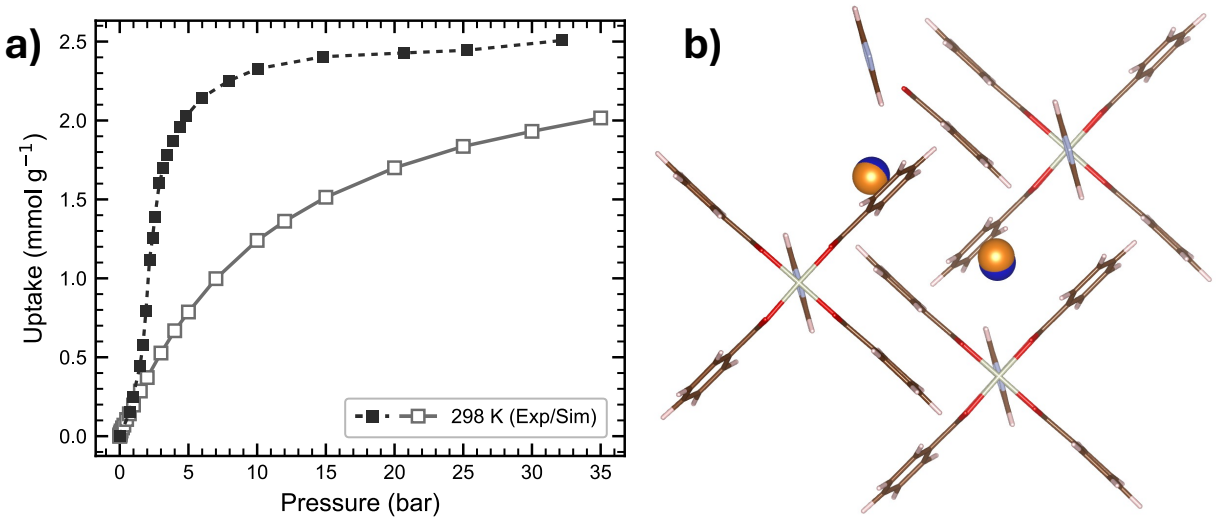

Figure S16. Comparison of binding site positions (experimental and simulated at 298 K, 80 bar) with Ar adsorption isotherms measured at 298 K for $[Rh_2(bza)_4(pyz)]_n$. Experimental binding sites are shown as orange spheres, and simulated binding sites are shown as blue spheres.

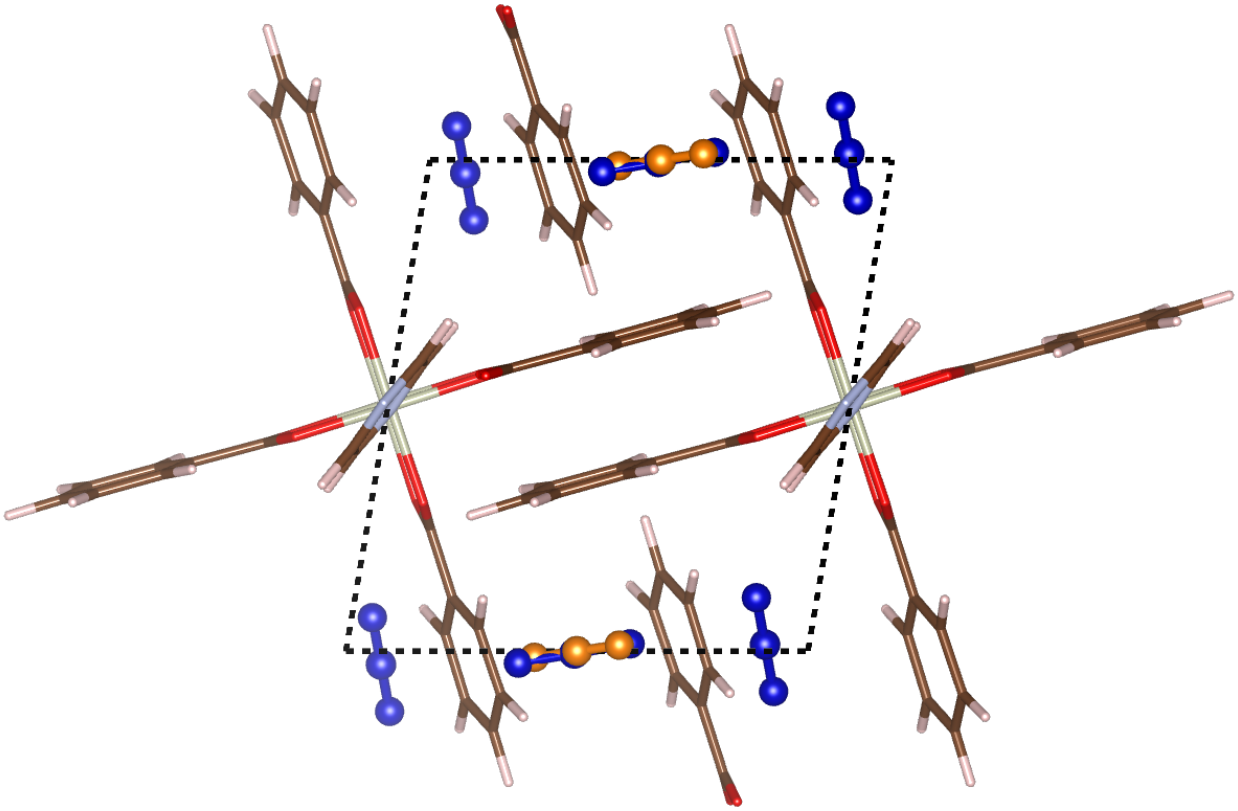

Figure S17. Comparison of binding site positions (experimental and simulated at 298 K, 35 bar) of CO_2 in $[Rh_2(bza)_4(pyz)]_n$. Experimental binding sites are shown as orange spheres, and simulated binding sites are shown as blue spheres.

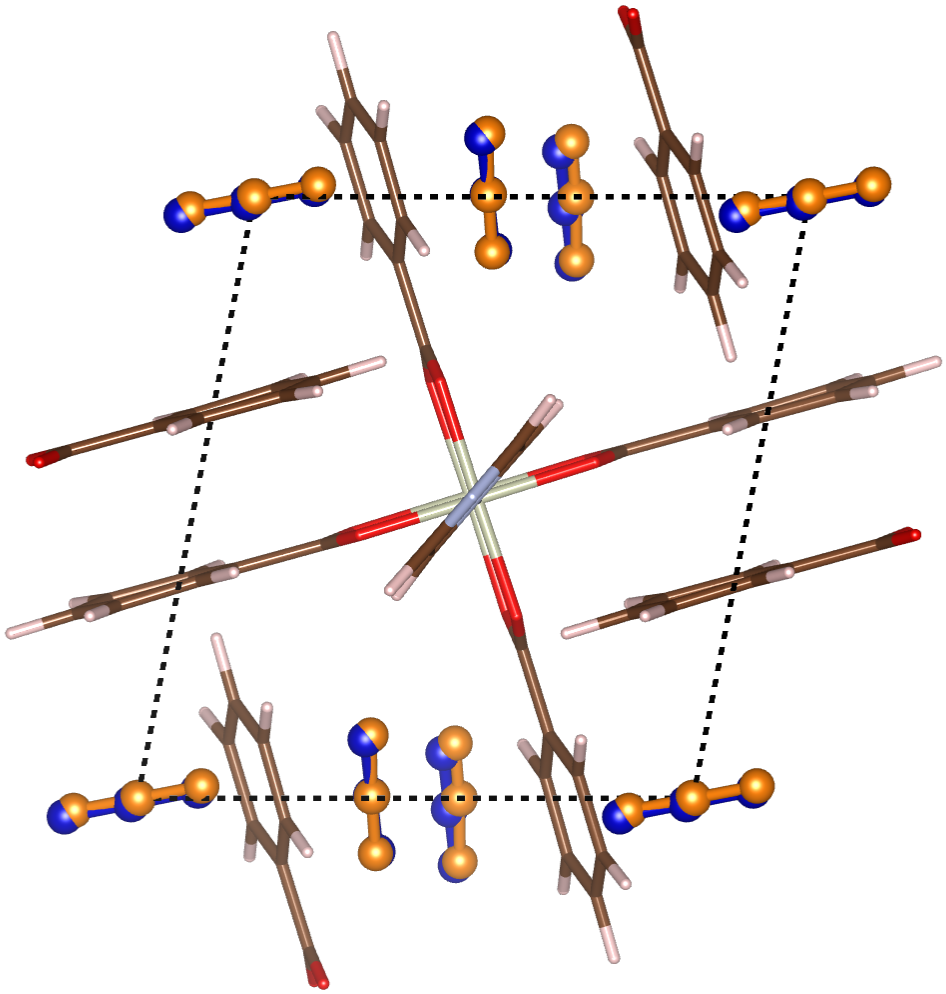

Figure S18. Comparison of binding site positions (experimental and simulated at 93 K, 1.01 bar) of CO_2 in ($[Rh_2(O_2CPh)_4(pyz)]_n$). Experimental binding sites are shown as orange spheres, and simulated binding sites are shown as blue spheres.

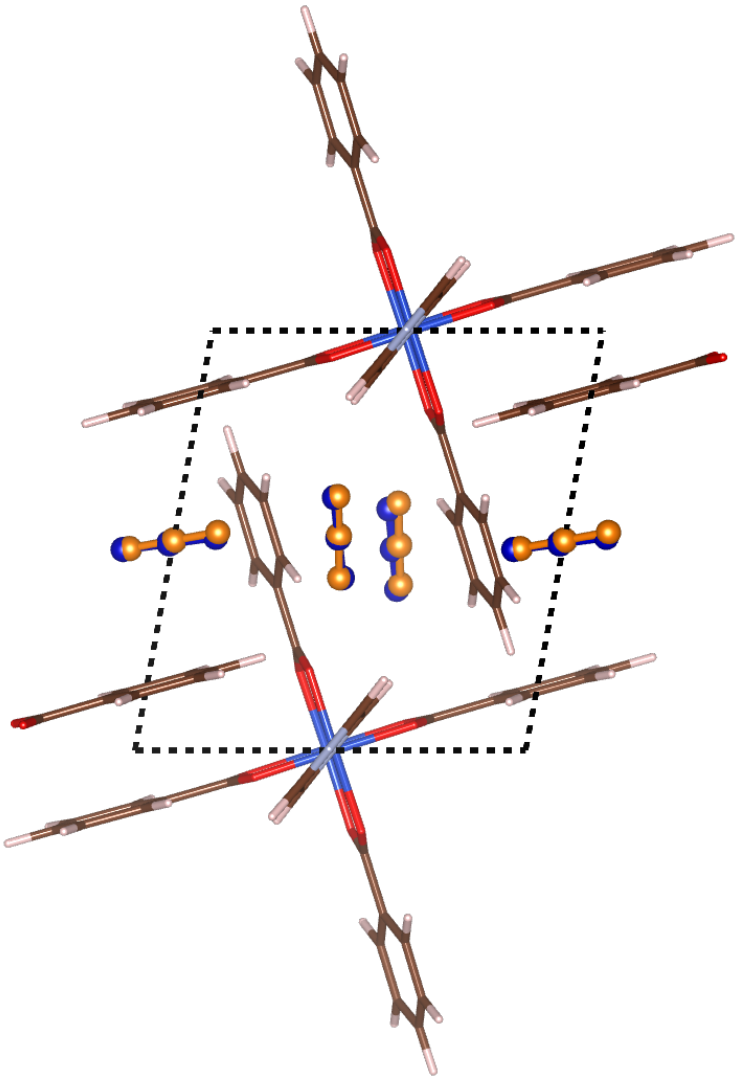

Figure S19. Comparison of binding site positions (experimental and simulated at 193 K, 1.01 bar) of CO_2 in $[Cu_2(bza)_4(pyz)]_n$. Experimental binding sites are shown as orange spheres, and simulated binding sites are shown as blue spheres.

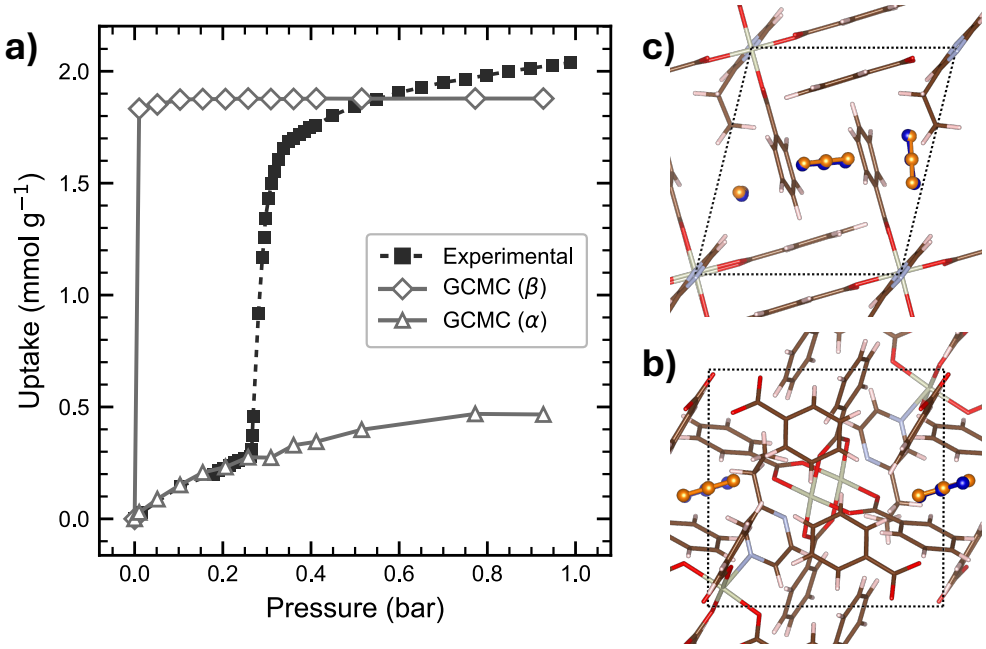

Figure S20. Comparison of binding site positions (experimental and simulated at 298 K and 64 bar in subfigure (c), 90 K and 36 bar in subfigure (b)) with CO_2 adsorption isotherms measured at 195 K for the flexible MOF $[Rh_2(bza)_4(2\text{-epyz})]_n$. Experimental binding sites are shown as orange spheres, and simulated binding sites are shown as blue spheres.

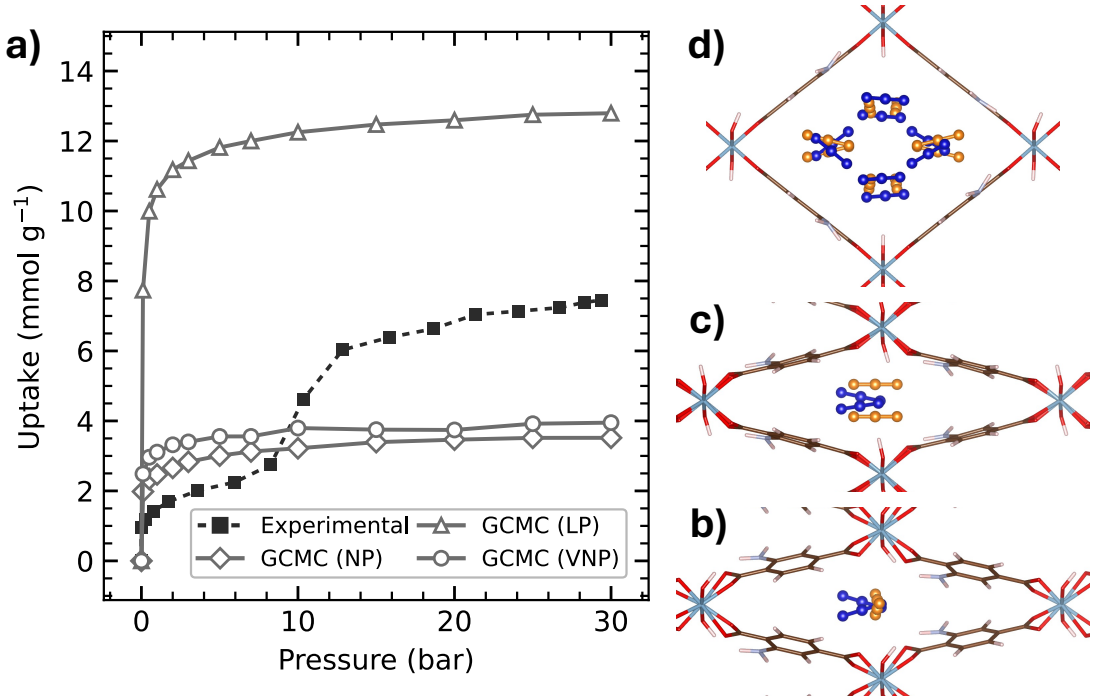

Figure S21. Comparison of binding site positions (experimental and simulated at 253 K, 3 bar (b), 9.5 bar (c) and 18 bar (d)) with CO_2 adsorption isotherms measured at 283 K for the flexible MOF MIL-53(Al). Experimental binding sites are shown as orange spheres, and simulated binding sites are shown as blue spheres.

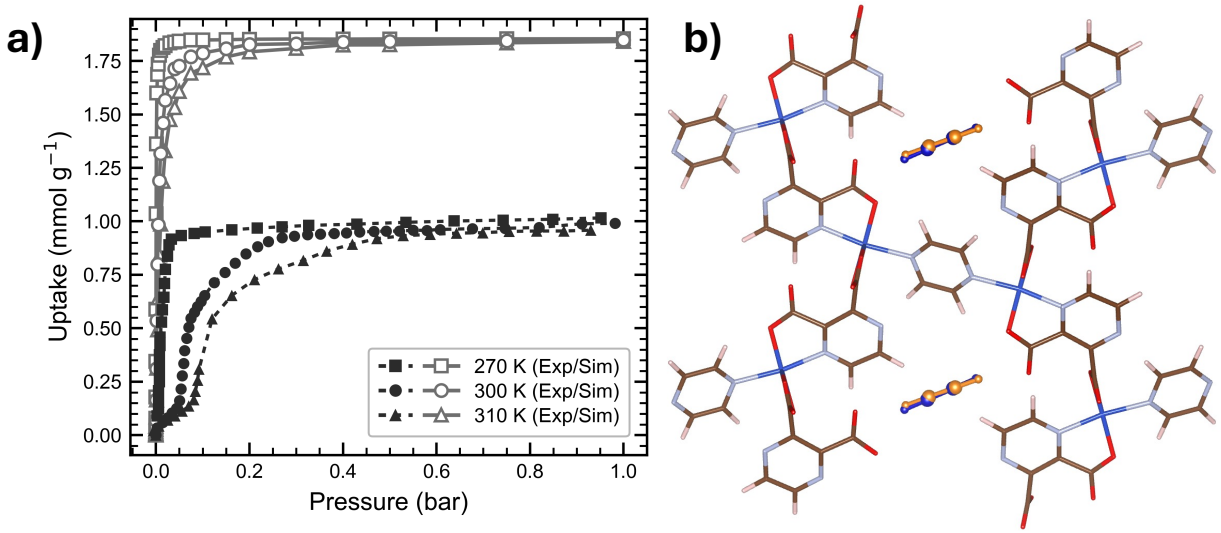

Figure S22. Comparison of binding site positions (experimental and simulated at 170 K, 0.1 bar) with C_2H_2 adsorption isotherms measured at 270 K, 300 K and 310 K for CPL-1. Experimental binding sites are shown as orange spheres, and simulated binding sites are shown as blue spheres.

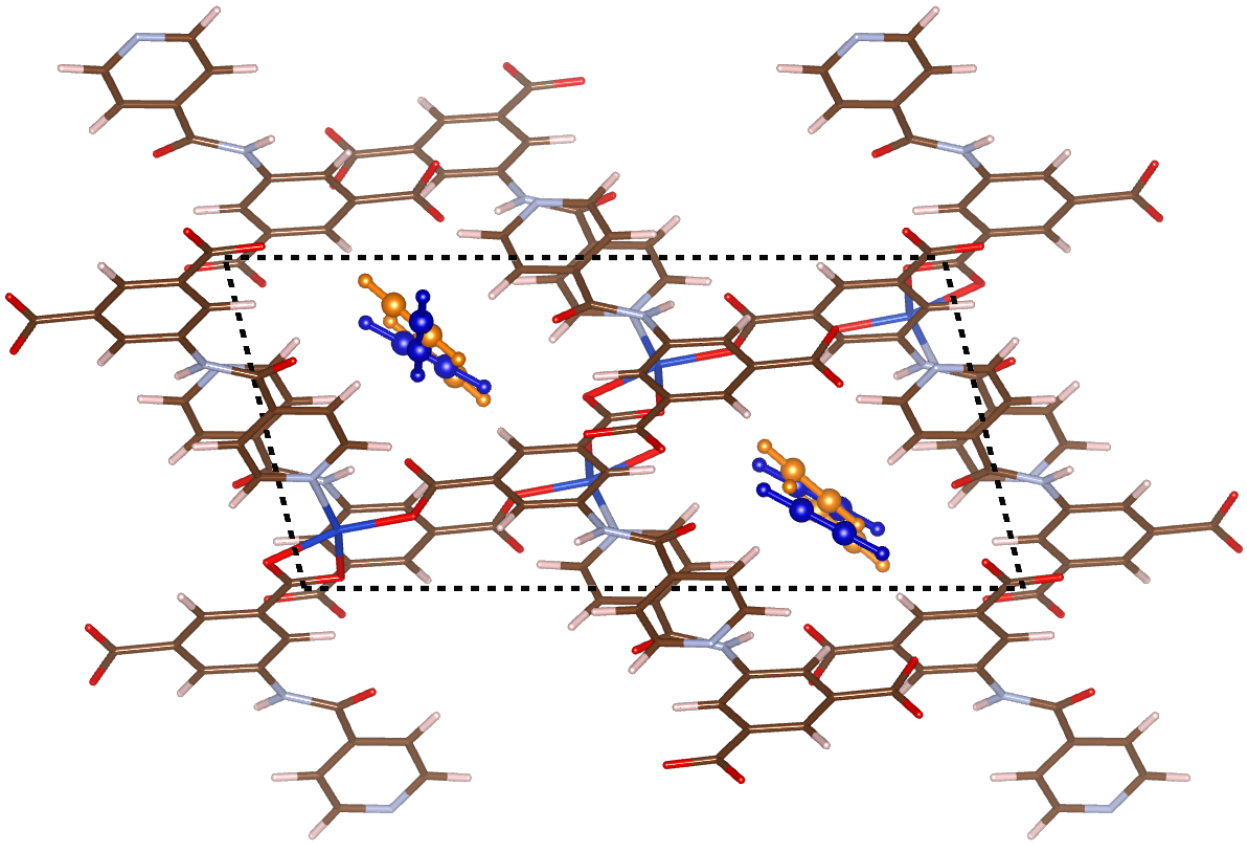

Figure S23. Comparison of binding site positions (experimental and simulated at 110 K, 0.18 bar) of C_2H_2 in INAIP-Cu. Experimental binding sites are shown as orange spheres, and simulated binding sites are shown as blue spheres.

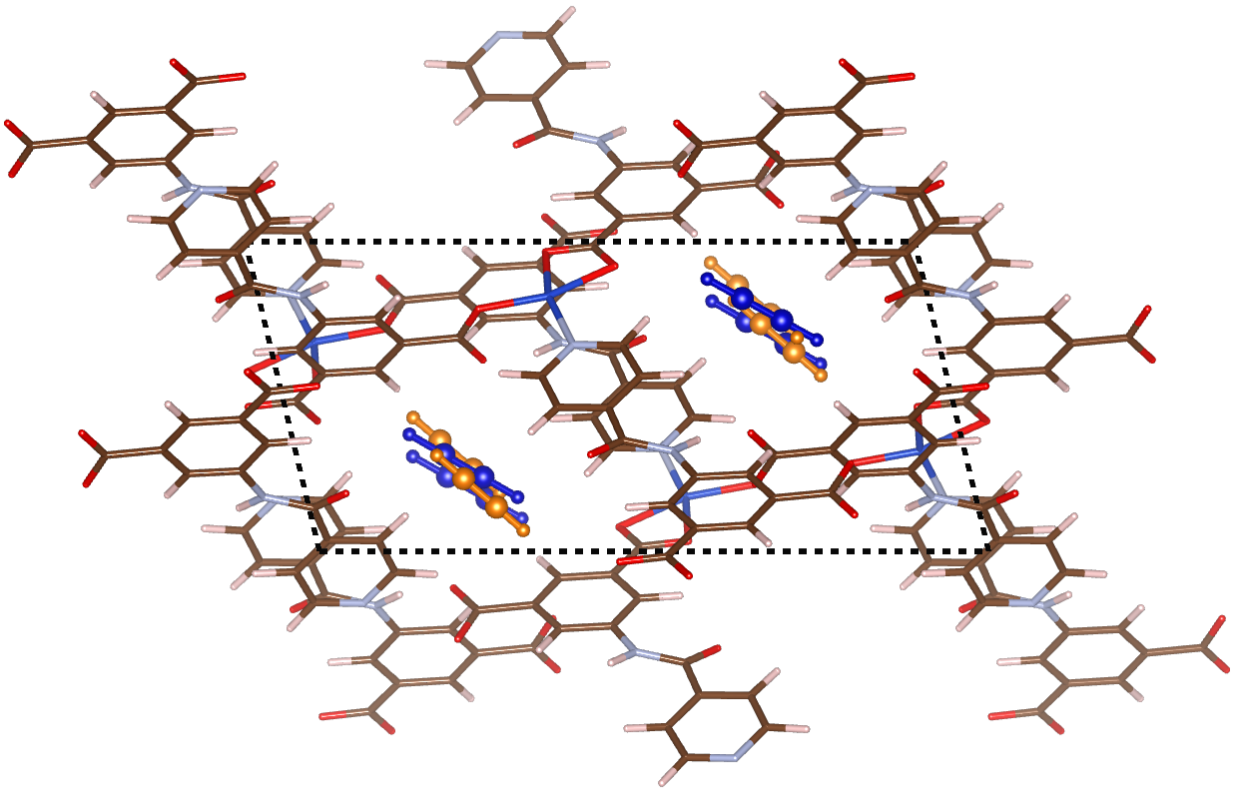

Figure S24. Comparison of binding site positions (experimental and simulated at 153 K, 0.85 bar) of C_2H_2 in INAIP-Cu. Experimental binding sites are shown as orange spheres, and simulated binding sites are shown as blue spheres.

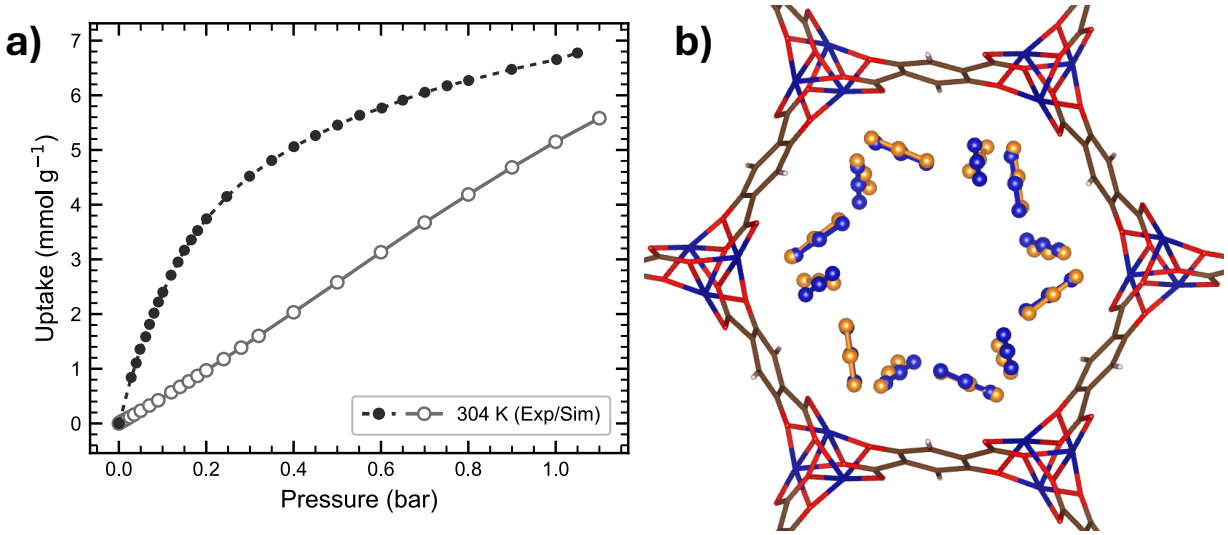

Figure S25. Comparison of binding site positions (experimental and simulated at 196 K, 1.06 bar) with CO_2 adsorption isotherms measured at 304 K for MOF-74(Co). Experimental binding sites are shown as orange spheres, and simulated binding sites are shown as blue spheres.

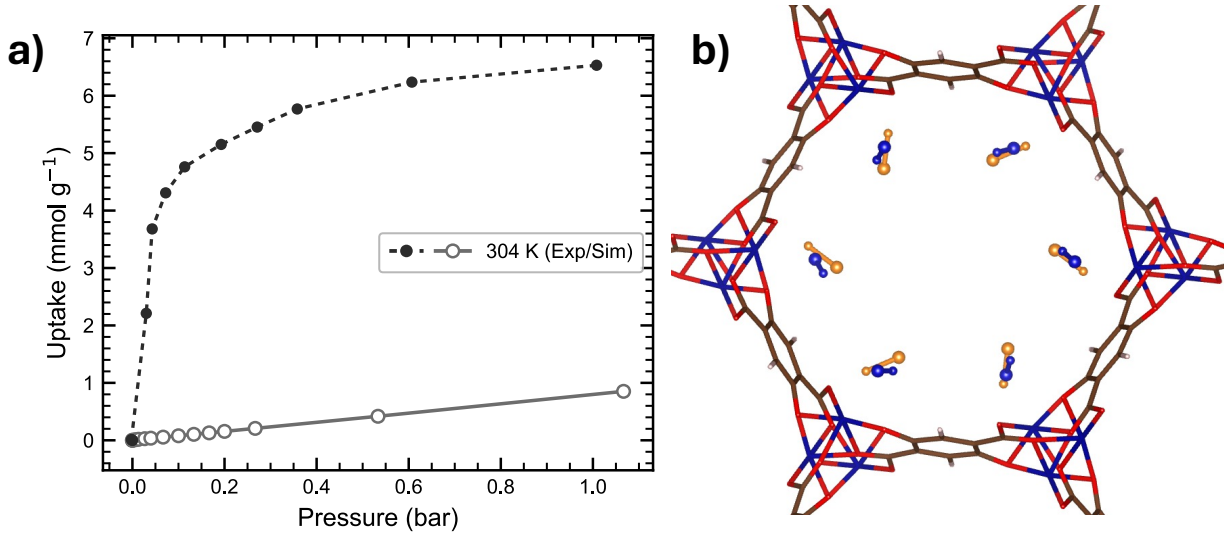

Figure S26. Comparison of binding site positions (experimental and simulated at 298 K, 1.01 bar) with NO adsorption isotherms measured at 304 K for MOF-74(Co). Experimental binding sites are shown as orange spheres, and simulated binding sites are shown as blue spheres. The nitrogen atoms are represented as smaller spheres to distinguish orientation.

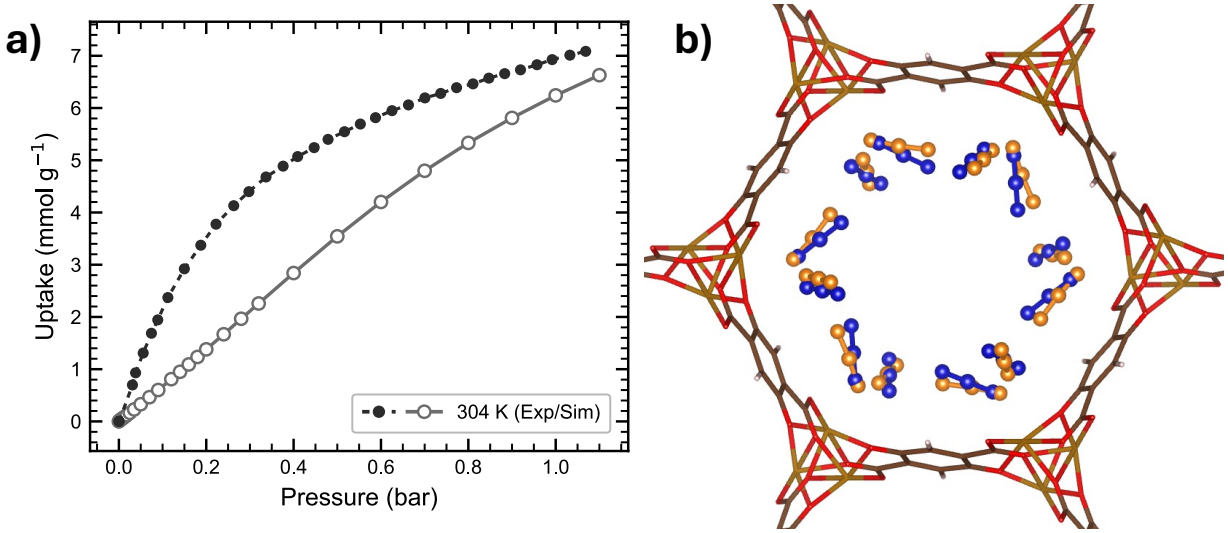

Figure S27. Comparison of binding site positions (experimental and simulated at 298 K, 1.01 bar) with CO_2 adsorption isotherms measured at 304 K for MOF-74(Fe). Experimental binding sites are shown as orange spheres, and simulated binding sites are shown as blue spheres.

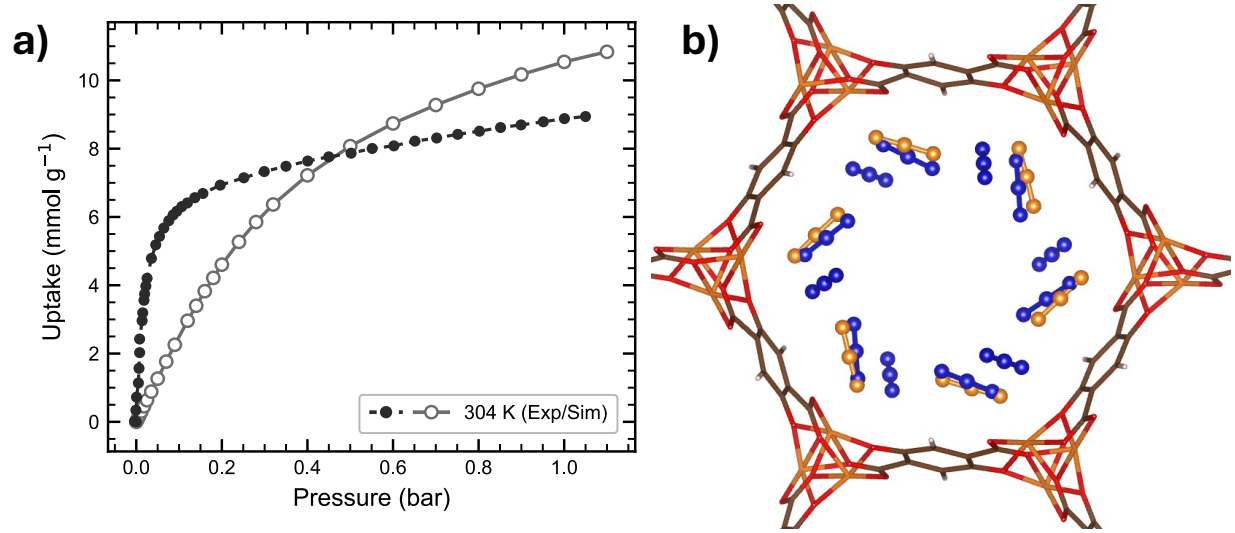

Figure S28. Comparison of binding site positions (experimental and simulated at 196 K, 1.06 bar) with CO_2 adsorption isotherms measured at 304 K for MOF-74(Mg). Experimental binding sites are shown as orange spheres, and simulated binding sites are shown as blue spheres.

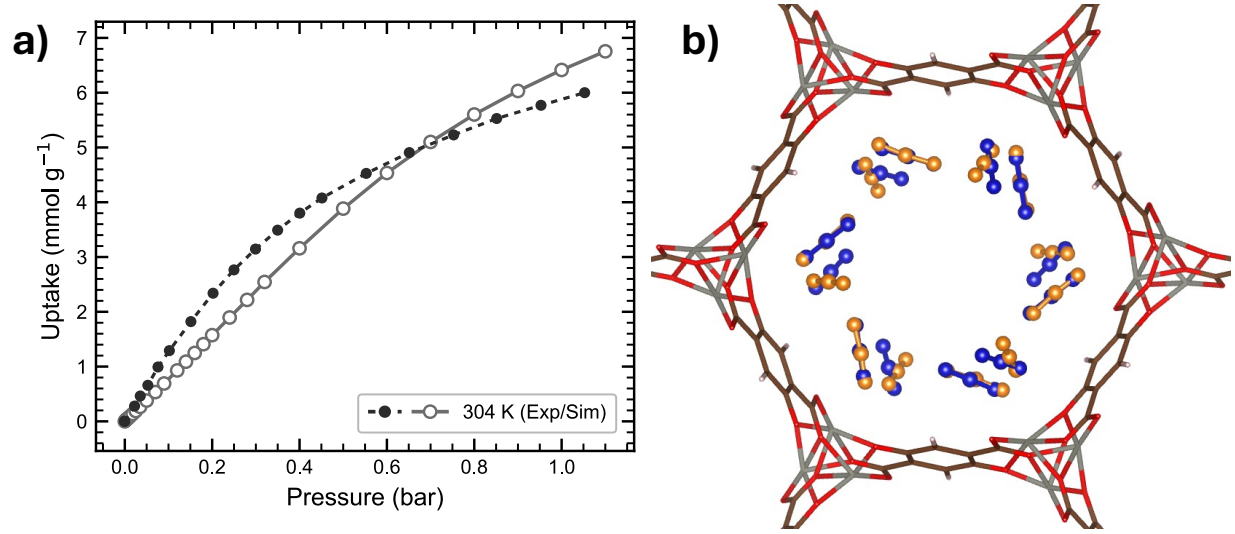

Figure S29. Comparison of binding site positions (experimental and simulated at 196 K, 1.06 bar) with CO_2 adsorption isotherms measured at 304 K for MOF-74(Zn). Experimental binding sites are shown as orange spheres, and simulated binding sites are shown as blue spheres.

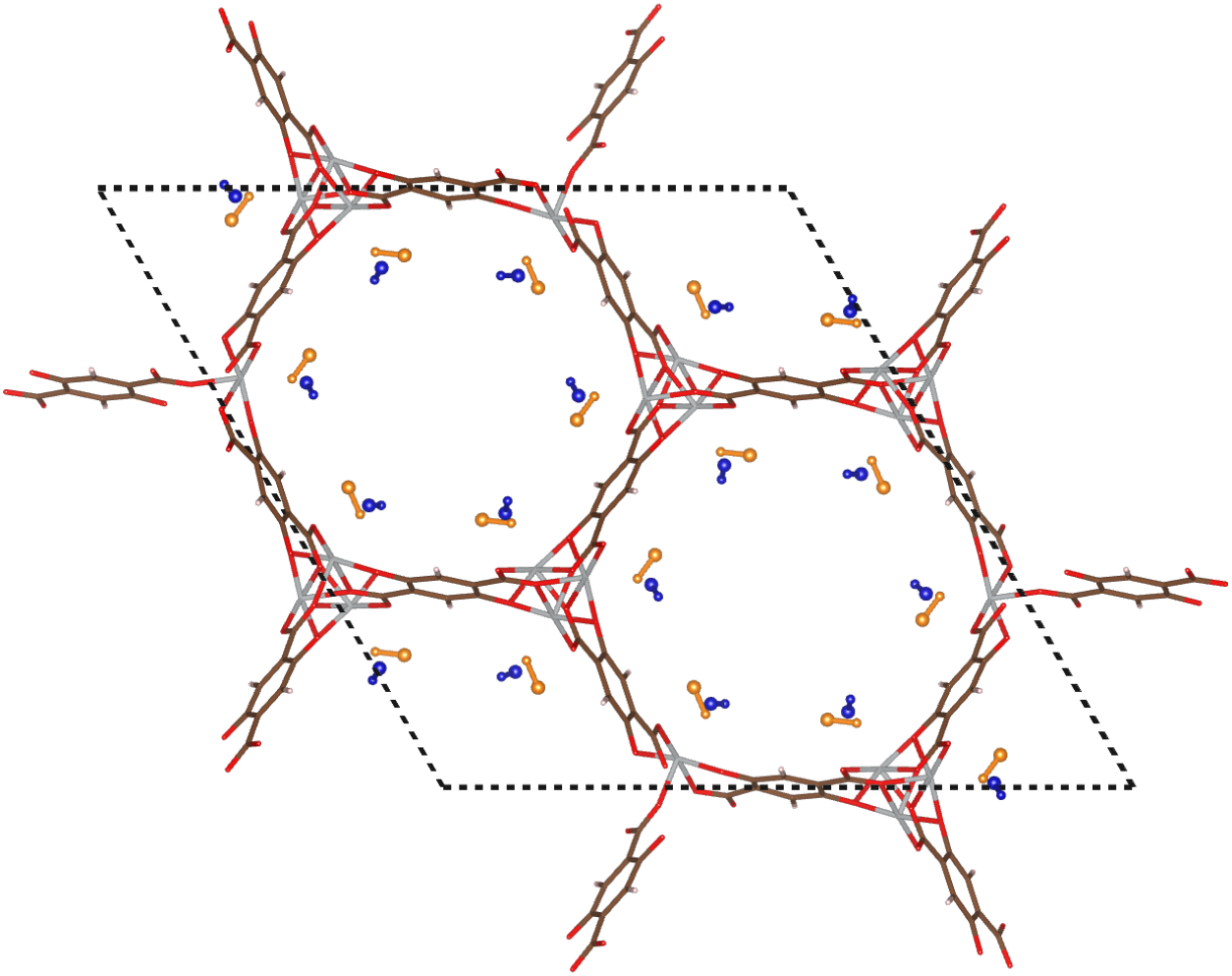

Figure S30. Comparison of binding site positions (experimental and simulated at 196 K, 0.4 bar) of NO in MOF-74(Ni) (OMS). Experimental binding sites are shown as orange spheres, and simulated binding sites are shown as blue spheres. The nitrogen atoms are represented as smaller spheres to distinguish orientation.

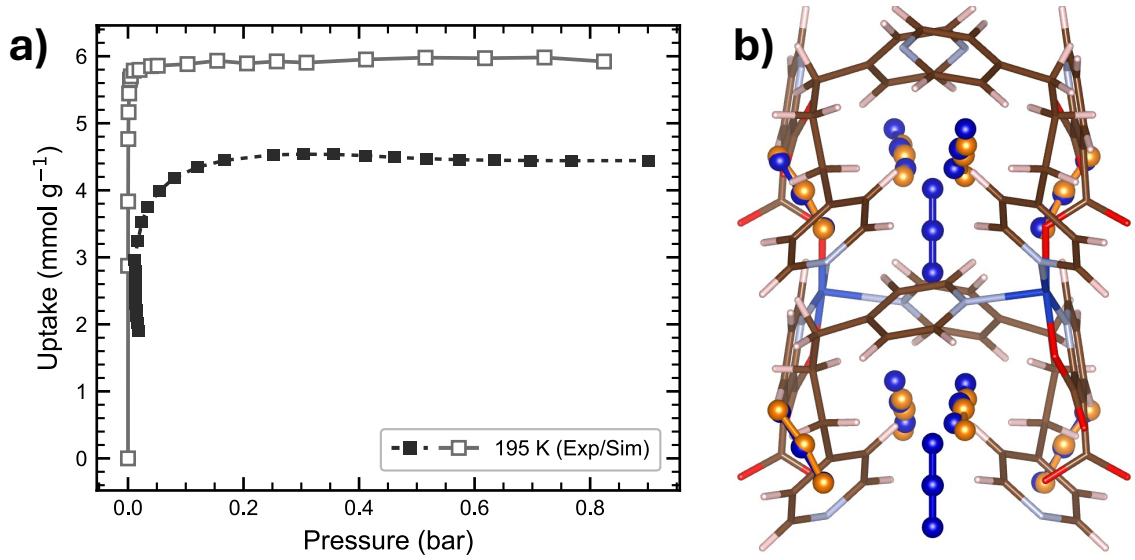

Figure S31. Comparison of binding site positions (experimental and simulated at 193 K, 1.01 bar) with CO_2 adsorption isotherms measured at 195 K for $[Cu_2(pyrdc)_2(bpp)_2]_n$. Experimental binding sites are shown as orange spheres, and simulated binding sites are shown as blue spheres.

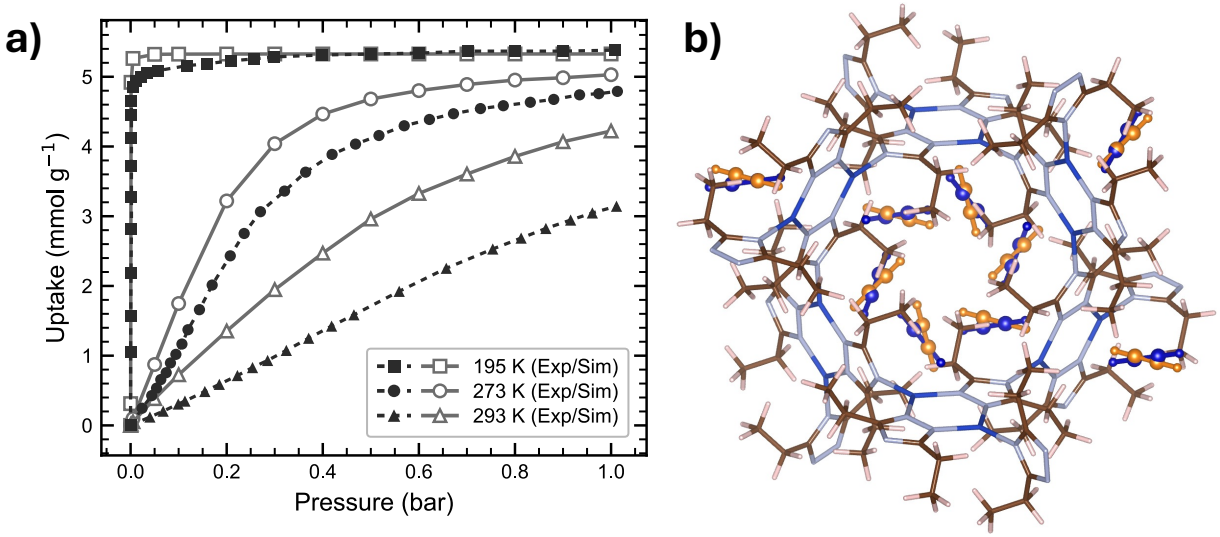

Figure S32. Comparison of binding site positions (experimental and simulated at 195 K, 10.13 bar) with C_2H_2 adsorption isotherms measured at 195 K, 273 K and 293 K for MAF-2(Zn). Experimental binding sites are shown as orange spheres, and simulated binding sites are shown as blue spheres.

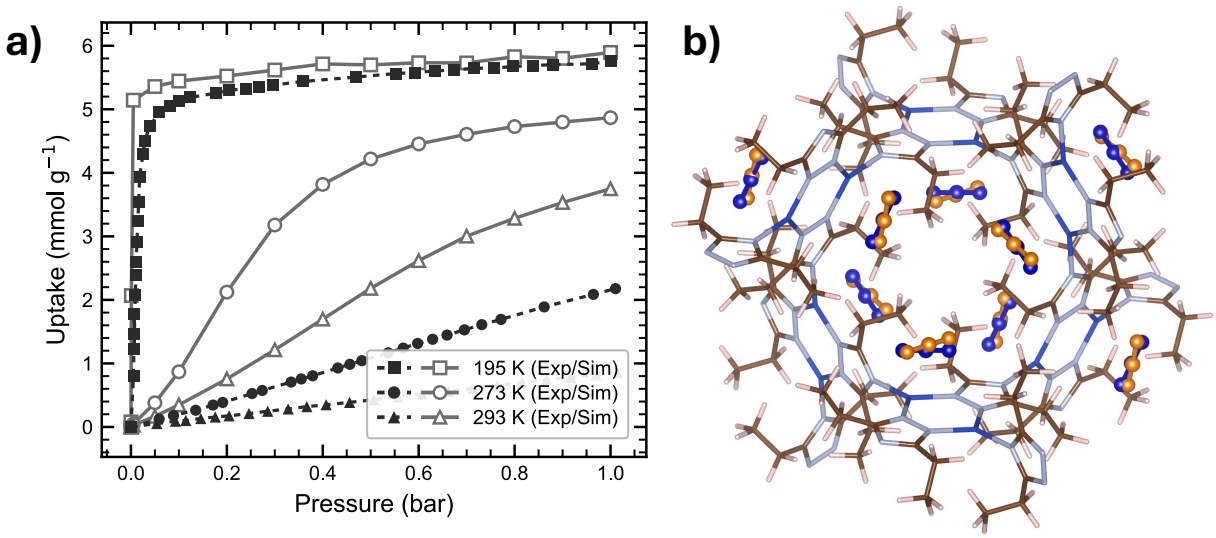

Figure S33. Comparison of binding site positions (experimental and simulated at 195 K, 20.27 bar) with CO_2 adsorption isotherms measured at 195 K, 273 K and 293 K for MAF-2(Zn). Experimental binding sites are shown as orange spheres, and simulated binding sites are shown as blue spheres.

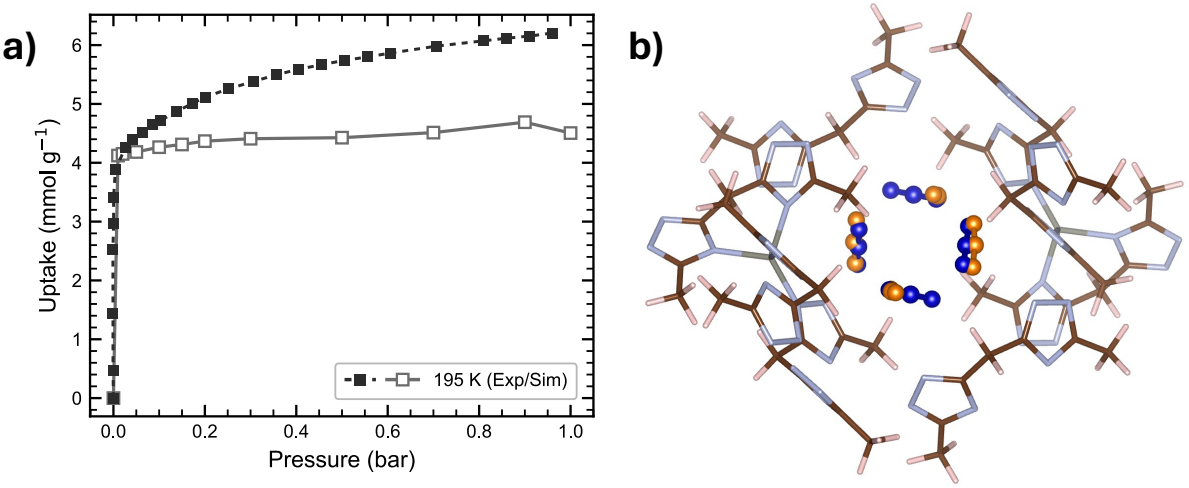

Figure S34. Comparison of binding site positions (experimental and simulated at 195 K, 0.79 bar) with CO_2 adsorption isotherms measured at 195 K for MAF-23(Zn). Experimental binding sites are shown as orange spheres, and simulated binding sites are shown as blue spheres.

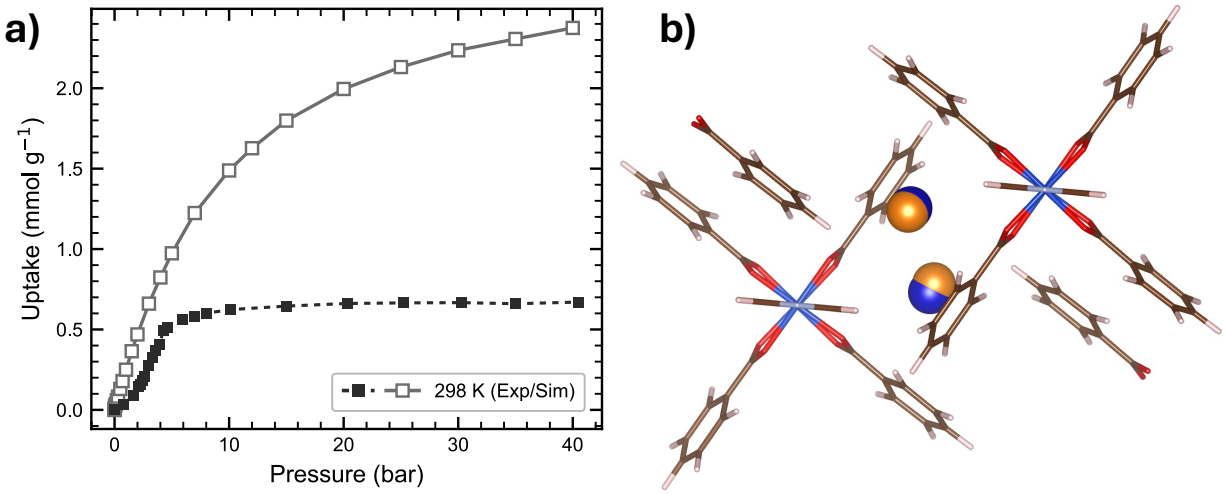

Figure S35. Comparison of binding site positions (experimental and simulated at 298 K, 100 bar) with Ar adsorption isotherms measured at 298 K for $[Cu_2(bza)_4(pyz)]_n$. Experimental binding sites are shown as orange spheres, and simulated binding sites are shown as blue spheres.

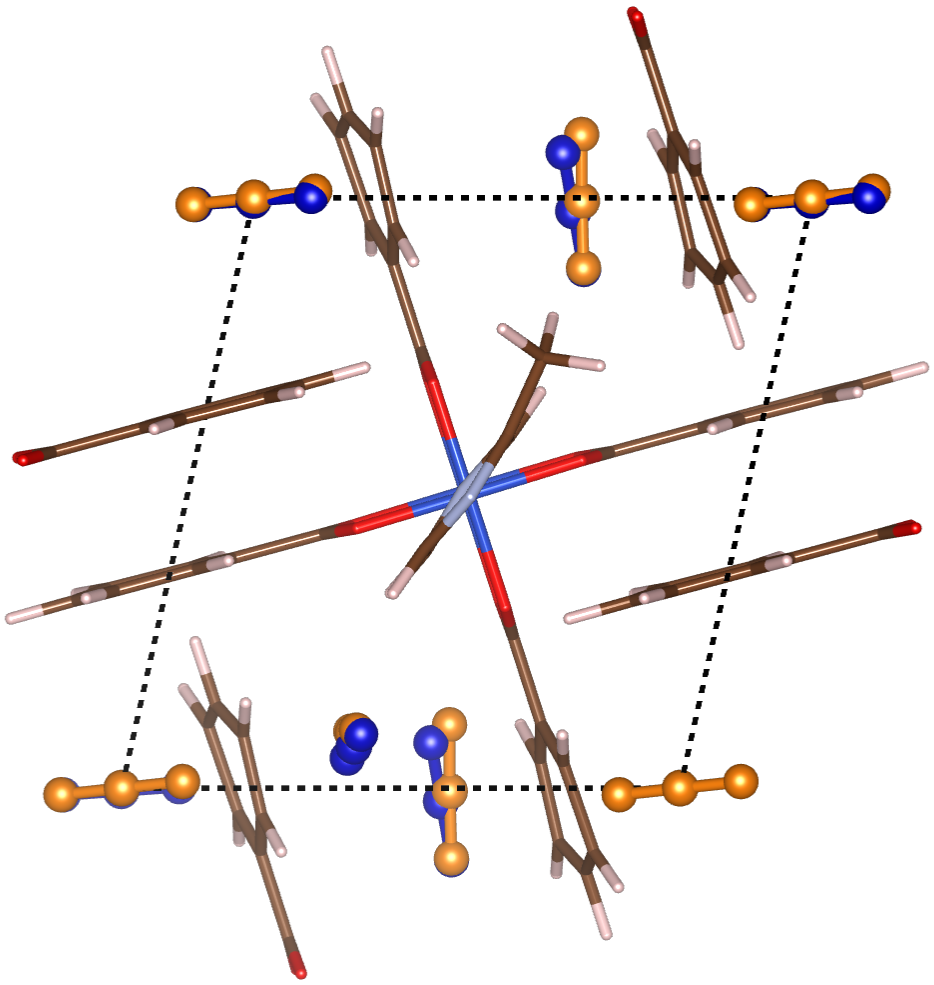

Figure S36. Comparison of binding site positions (experimental and simulated at 90 K, 1 bar) of CO_2 in $[Cu_2(bza)_4(methyl\text{-}pyz)]_n$. Experimental binding sites are shown as orange spheres, and simulated binding sites are shown as blue spheres.

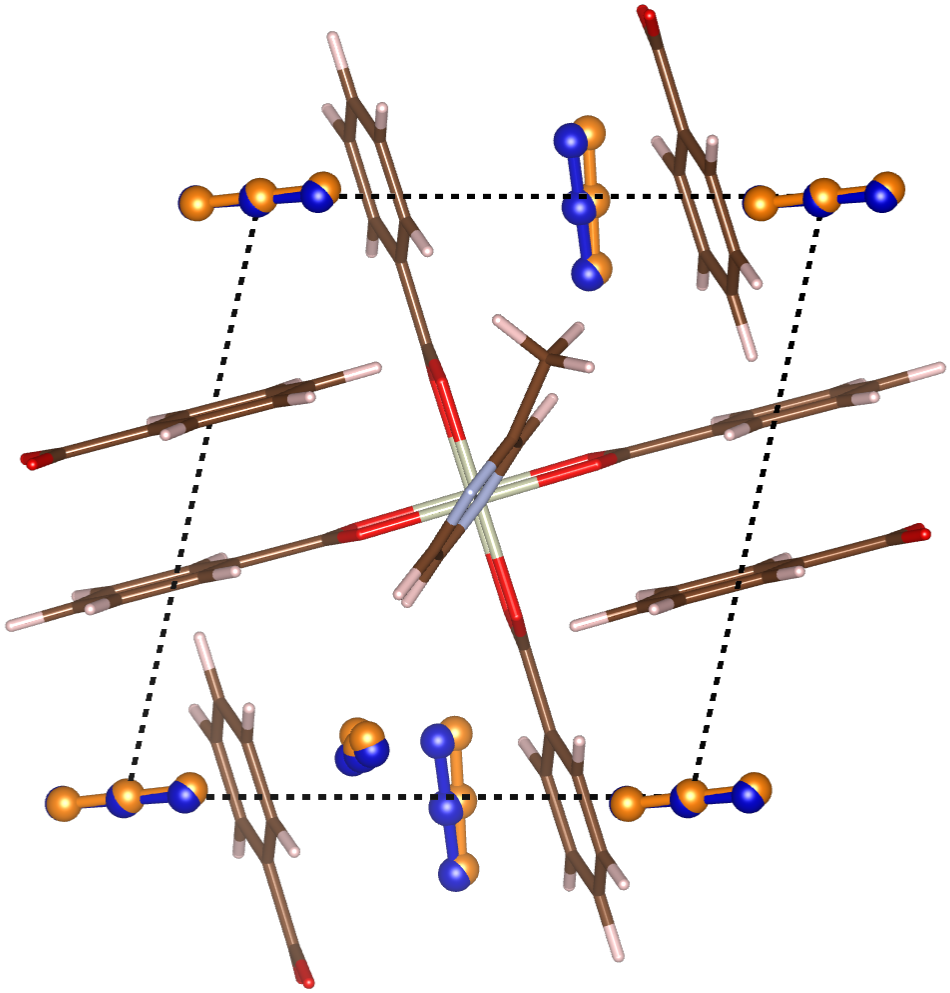

Figure S37. Comparison of binding site positions (experimental and simulated at 90 K, 1 bar) of CO_2 in $[Rh_2(bza)_4(methyl\text{-}pyz)]_n$. Experimental binding sites are shown as orange spheres, and simulated binding sites are shown as blue spheres.

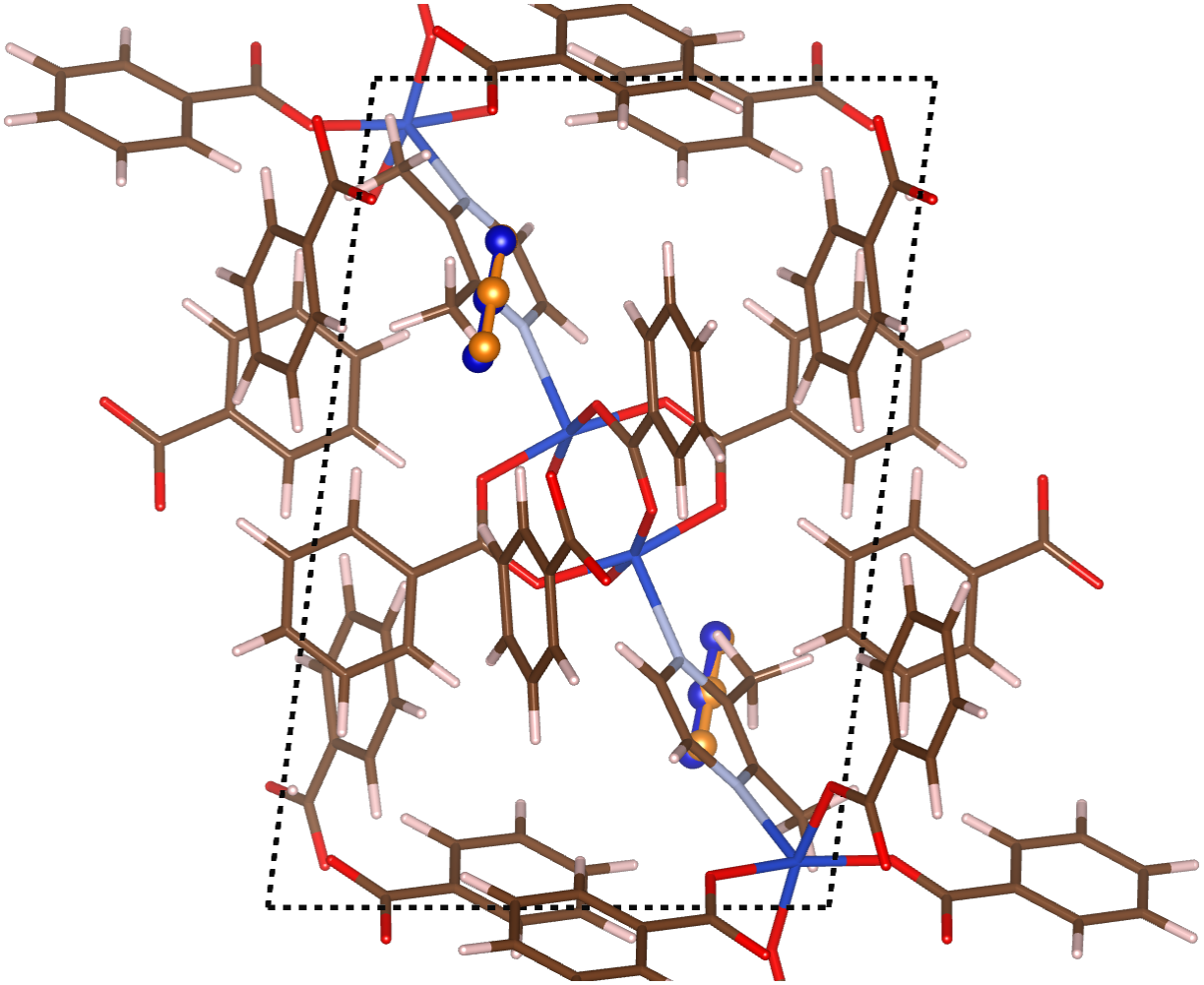

Figure S38. Comparison of binding site positions (experimental and simulated at 90 K, 1 bar) of CO_2 in $[Cu_2(bza)_4(dimethyl\text{-}pyz)]_n$. Experimental binding sites are shown as orange spheres, and simulated binding sites are shown as blue spheres.

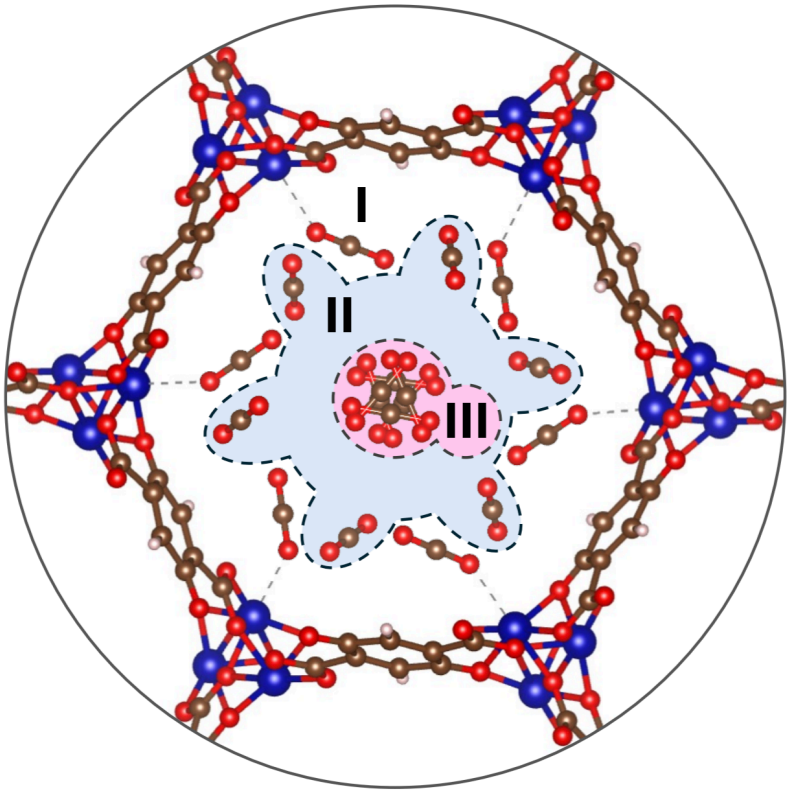

Figure S39. Primary (I), secondary (II), and tertiary (III) binding sites of MOF-74(Co), as determined by GCMC simulations. Queen, et al.[19] suggests a highly disordered tertiary site at the centre of the MOF pore observed with SCXRD and NPD, which is recovered from our GCMC simulations.

7. References

(1) Perdew, J. P. Generalized Gradient Approximation Made Simple. *Phys. Rev. Lett.* **1996**, *77* (18), 3865–3868. https://doi.org/10.1103/PhysRevLett.77.3865.

(2) Grimme, S.; Antony, J.; Ehrlich, S.; Krieg, H. A Consistent and Accurate Ab Initio Parametrization of Density Functional Dispersion Correction (DFT-D) for the 94 Elements H-Pu. *J. Chem. Phys.* **2010**, *132* (15), 154104. https://doi.org/10.1063/1.3382344.

(3) Kresse, G.; Joubert, D. From Ultrasoft Pseudopotentials to the Projector Augmented-Wave Method. *Phys. Rev. B* **1999**, *59* (3), 1758–1775. https://doi.org/10.1103/PhysRevB.59.1758.

(4) Blöchl, P. E. Projector Augmented-Wave Method. *Phys. Rev. B* **1994**, *50* (24), 17953–17979. https://doi.org/10.1103/PhysRevB.50.17953.

(5) Campañá, C.; Mussard, B.; Woo, T. K. Electrostatic Potential Derived Atomic Charges for Periodic Systems Using a Modified Error Functional. *J. Chem. Theory Comput.* **2009**, *5* (10), 2866–2878. https://doi.org/10.1021/ct9003405.

(6) Manz, T. A.; Limas, N. G. Introducing DDEC6 Atomic Population Analysis: Part 1. Charge Partitioning Theory and Methodology. *RSC Adv.* **2016**, *6* (53), 47771–47801. https://doi.org/10.1039/C6RA04656H.

(7) Berquist, E. Chargemol. https://github.com/berquist/chargemol.

(8) Li, Y.; Jin, X.; Moubarak, E.; Smit, B. A Refined Set of Universal Force Field Parameters for Some Metal Nodes in Metal–Organic Frameworks. *J. Chem. Theory Comput.* **2024**, *20* (23), 10540–10552. https://doi.org/10.1021/acs.jctc.4c01113.
(9) Mayo, S. L.; Olafson, B. D.; Goddard, W. A. DREIDING: A Generic Force Field for Molecular Simulations. *J. Phys. Chem.* **1990**, *94* (26), 8897–8909. https://doi.org/10.1021/j100389a010.
(10) García-Sánchez, A.; Ania, C. O.; Parra, J. B.; Dubbeldam, D.; Vlugt, T. J. H.; Krishna, R.; Calero, S. Transferable Force Field for Carbon Dioxide Adsorption in Zeolites. *J. Phys. Chem. C* **2009**, *113* (20), 8814–8820. https://doi.org/10.1021/jp810871f.
(11) Fischer, M.; Hoffmann, F.; Fröba, M. New Microporous Materials for Acetylene Storage and C2H2/CO2 Separation: Insights from Molecular Simulations. *ChemPhysChem* **2010**, *11* (10), 2220–2229. https://doi.org/10.1002/cphc.201000126.
(12) Horn, H. W.; Swope, W. C.; Pitera, J. W.; Madura, J. D.; Dick, T. J.; Hura, G. L.; Head-Gordon, T. Development of an Improved Four-Site Water Model for Biomolecular Simulations: TIP4P-Ew. *J. Chem. Phys.* **2004**, *120* (20), 9665–9678. https://doi.org/10.1063/1.1683075.
(13) Zhou, Z.; Todd, B. D.; Travis, K. P.; Sadus, R. J. A Molecular Dynamics Study of Nitric Oxide in Water: Diffusion and Structure. *J. Chem. Phys.* **2005**, *123* (5), 054505. https://doi.org/10.1063/1.1992482.
(14) Martin, M. G.; Siepmann, J. I. Transferable Potentials for Phase Equilibria. 1. United-Atom Description of n-Alkanes. *J. Phys. Chem. B* **1998**, *102* (14), 2569–2577. https://doi.org/10.1021/jp972543+.
(15) Boato, G.; Casanova, G. A Self-Consistent Set of Molecular Parameters for Neon, Argon, Krypton and Xenon. *Physica* **1961**, *27* (6), 571–589. https://doi.org/10.1016/0031-8914(61)90072-6.
(16) Kadantsev, E. S.; Boyd, P. G.; Daff, T. D.; Woo, T. K. Fast and Accurate Electrostatics in Metal Organic Frameworks with a Robust Charge Equilibration Parameterization for High-Throughput Virtual Screening of Gas Adsorption. *J. Phys. Chem. Lett.* **2013**, *4* (18), 3056–3061. https://doi.org/10.1021/jz401479k.
(17) Luo, J.; Said, O. B.; Xie, P.; Gibaldi, M.; Burner, J.; Pereira, C.; Woo, T. K. MEPO-ML: A Robust Graph Attention Network Model for Rapid Generation of Partial Atomic Charges in Metal-Organic Frameworks. *Npj Comput. Mater.* **2024**, *10* (1), 224. https://doi.org/10.1038/s41524-024-01413-4.
(18) Main, R. M.; Ettlinger, R.; Tajnšek, T. K.; Brako-Amoafo, D. A.; Stanzione, M. G.; Duncan, M. J.; Ettlinger, P.; Lawrence, G. B.; Warren, M. R.; Heard, C. J.; Morris, R. E. In Situ Single-Crystal X-Ray Diffraction Studies of an Anomalous Nitric Oxide Adsorption in a Partially Activated Metal–Organic Framework. *J. Am. Chem. Soc.* **2025**, *147* (34), 31260–31269. https://doi.org/10.1021/jacs.5c10395.
(19) Queen, W. L.; Hudson, M. R.; Bloch, E. D.; Mason, J. A.; Gonzalez, M. I.; Lee, J. S.; Gygi, D.; Howe, J. D.; Lee, K.; Darwish, T. A.; James, M.; Peterson, V. K.; Teat, S. J.; Smit, B.; Neaton, J. B.; Long, J. R.; Brown, C. M. Comprehensive Study of Carbon Dioxide Adsorption in the Metal–Organic Frameworks M2(Dobdc) (M = Mg, Mn, Fe, Co, Ni, Cu, Zn). *Chem. Sci.* **2014**, *5* (12), 4569–4581. https://doi.org/10.1039/C4SC02064B.